

Persistent homology transform for modeling shapes and surfaces

KATHARINE TURNER[†]

Department of Mathematics, University of Chicago, Chicago, IL 60637, USA

[†]Corresponding author. Email: kate@math.uchicago.edu

SAYAN MUKHERJEE

Departments of Statistical Science, Computer Science, and Mathematics, Duke University, Durham, NC 27708, USA

AND

DOUG M. BOYER

Department of Evolutionary Anthropology, Duke University, Durham, NC 27708, USA

[Received on 28 October 2013; revised on 26 October 2014; accepted on 28 October 2014]

We introduce a statistic, the persistent homology transform (PHT), to model surfaces in \mathbb{R}^3 and shapes in \mathbb{R}^2 . This statistic is a collection of persistence diagrams—multiscale topological summaries used extensively in topological data analysis. We use the PHT to represent shapes and execute operations such as computing distances between shapes or classifying shapes. We provide a constructive proof that the map from the space of simplicial complexes in \mathbb{R}^3 into the space spanned by this statistic is injective. This implies that we can use it to determine a metric on the space of piecewise linear shapes. Stability results justify that we can approximate this metric using finitely many persistence diagrams. We illustrate the utility of this statistic on simulated and real data.

Keywords: persistence homology; surfaces; shape spaces; shape statistics.

1. Introduction

We introduce here a new tool, the persistent homology transform (PHT), to perform statistical shape analysis on objects in \mathbb{R}^3 and shapes in \mathbb{R}^2 . This result is of interest to three communities, the shape statistics community [7,18,24,25], the topological data analysis (TDA) community [11,12,14,20,21], and applied statisticians and domain researchers modeling shapes including medical imaging [2,38] and morphology [7,8,45].

Fitting curves and surfaces to model shapes has many applications in a variety of fields. A concrete example of central interest to one of the authors is computing the distance between heel bones in primates to generate a tree and comparing this tree with a tree generated from the genetic distances between the primate species [9]. The central problem in almost all approaches to modeling surfaces and shapes is obtaining a representation of the shape that can be used in statistical models.

We show that a collection of persistence diagrams—multiscale topological summaries used extensively in TDA—completely describe a shape or surface. This is of interest to the TDA community since it is the first formal demonstration that persistent homology [12,20], the dominant tool used in TDA, does not result in the loss of information.

Statistical models of shapes (characterized as a set of landmarks) were pioneered in the works of Kendall and Bookstein [7,24,25]. Almost all statistical models start with a set of landmarks provided by the user as an initialization step; a probability model is then placed on these landmarks.

However, from the perspective of the likelihood principal [3] statistical inference should proceed from a probability model on the shapes themselves, unless the landmarks are sufficient statistics for shapes. The central idea developed in this line of work was the shape space, a differentiable manifold often with appropriate Riemannian structures. See [2,5,6,17,35] for recent results on statistical analysis of shapes.

An alternative approach to modeling shapes comes from the formulation by Grenander [19]. In this formulation shapes are considered as points on an infinite-dimensional manifold and variation in shape is modeled by the action of Lie groups on these manifolds. This is a very appealing paradigm but is computationally intensive and requires the parameterization of the shape manifold.

Our approach is to transform the shapes instead. Ideas in integral geometry that have been used to model surfaces and random fields [37,43,44] as well as point processes [16,30,32,37]. The central idea to the integral geometric approach was to study invariant integral transforms from the space of functions on surfaces or shapes to spaces of functions that are more convenient for analysis such as functions on an interval of the real line. The idea is that one can more easily manipulate, compute and model in the transformed space. See [26] for details on classic ideas in integral geometry including Minkowski functionals and Hadwiger integrals.

A classic example of a widely used integral transform is the Radon transform. We consider a topological analog of the Radon transform. The results here are very related to the combination of the Radon transform with Euler calculus as studied in [33,34].

Another line of research we draw from is comparing shapes using multiscale topological summaries of data. The key idea we draw upon from this discipline is the elevation function [1,42], which was developed as an application of discrete Morse theory to problems in protein structure modeling.

We begin the paper with topological preliminaries and relevant definitions in Section 2. In Section 3, we first state and prove conditions under which the PHT is an injective transform. We then state injectivity results for the 0th dimensional PHT for surfaces that are homeomorphic to a sphere. We end the section with a discussion on the setting when the objects are not aligned and we have to quotient out translation, scaling and rotation as is normally done in shape statistics. In Section 4, we show the efficacy of our method for computing distances between shapes and surfaces in simulated data as well as real data. For the simulated data, we demonstrate that we can work with unaligned objects. We close with a discussion.

1.1 *A motivating example*

The classical problem in morphology of measuring distances between bones often is realized as measuring the distance between the surfaces of the bones. Historically, this problem has been very amenable to classical shape statistics as the information about a bone was stored as a set of landmark points on the bone and distances between the landmark points. However, with the increased prevalence of scanning technologies such as computerized tomography (CT) scans, bones are now often represented as meshes. In Fig. 1, we display a snapshot of the meshes of five teeth. Understanding variation in a set of bones or teeth by providing estimates of distances between the surfaces in an automated fashion [8,9,23] would be of great practical importance.

In [8], a procedure to measure distances between surfaces, such as the boundary surfaces of teeth, was developed using conformal geometry to construct flattened representations of pairs of surfaces

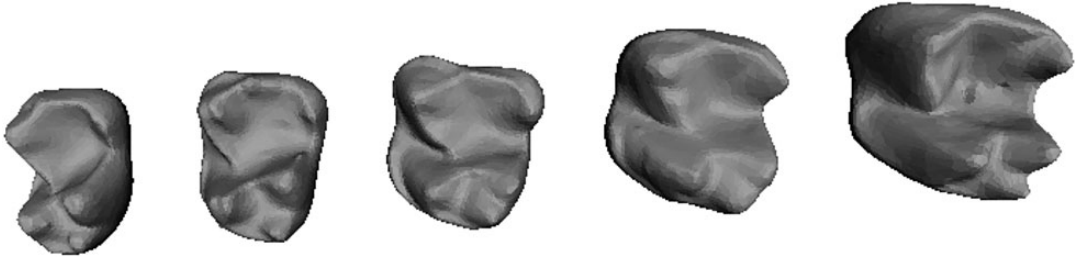


FIG. 1. Images of the meshes of five teeth. A common problem in morphology is to measure distances between these five teeth.

followed by continuous Procrustes distance [29] to measure the distance between the surfaces. A setting where this approach will have problems is when one wants to measure distances between objects that are not isomorphic. For example, if one of the teeth were broken, then generating a conformal map from the broken region of the tooth to the corresponding intact region of the other tooth will be a problem.

We will apply the PHT to measure distances between surfaces. Specifically, in Section 4 we will use the PHT to measure distances between the heel bones of 106 primates. The basic approach will be to transform each bone using the PHT and use standard distances between persistence diagrams to measure pairwise distances between bones. We will then cluster these distances to propose evolutionary relations between the primate species. One utility of our approach is that we do not have to compute a correspondence between the bones, as is required in a conformal map. In the case, where correspondences are very unstable as would be the case when objects are not isomorphic, our procedure should be more robust.

2. Persistence diagrams and height functions

2.1 Definitions and topological preliminaries

Persistent homology is a computational method for measuring changes in the homology of a filtration of simplicial complexes. We first review the notion of a simplicial complex and simplicial homology. The computation of persistent homology requires a field, in general simplicial homology can be computed over any ring. In this paper, as in most of TDA, the field is \mathbb{Z}_2 to ease computations.

Simplices are the elementary objects on which we will operate. Examples are points, lines, triangles and k -dimensional generalizations. Formally, a k -simplex is the convex hull of $k + 1$ affinely independent points v_0, v_1, \dots, v_k and is denoted as $[v_0, v_1, \dots, v_k]$. For example, the 0-simplex $[v_0]$ is the vertex v_0 , the 1-simplex $[v_0, v_1]$ is the edge between the vertices v_0 and v_1 , and the 2-simplex $[v_0, v_1, v_2]$ is the triangle bordered by the edges $[v_0, v_1]$, $[v_1, v_2]$ and $[v_0, v_2]$.

A simplicial complex consists of simplices glued together with certain rules. To define the rules, we first define the face of a simplex. We call $[u_0, u_1, \dots, u_j]$ a *face* of $[v_0, v_1, \dots, v_k]$ if $\{u_0, u_1, \dots, u_j\} \subset \{v_0, v_1, \dots, v_k\}$. A *simplicial complex* M is a countable set of simplices such that

- (1) every face of a simplex in M is also in M ;
- (2) if two simplices σ_1, σ_2 are in M , then their intersection is either empty or a face of both σ_1 and σ_2 .

Given finite simplicial complex K , a *simplicial k -chain* is a formal linear combination (over \mathbb{Z}_2 in this paper) of k -simplices in K . The set of k -chains forms a vector space $C_k(K)$. We define the boundary map $\partial_k : C_k(K) \rightarrow C_{k-1}(K)$ as

$$\partial_k([v_0, v_1, \dots, v_k]) = \sum_{j=0}^k (-1)^j [v_0, \dots, v_{j-1}, v_{j+1}, \dots, v_k]$$

and extending linearly.

Elements of $B_k(K) = \text{im } \partial_{k+1}$ are called boundaries and elements of $Z_k(K) = \ker \partial_k$ are called cycles.¹ Direct computation shows $\partial_{k+1} \circ \partial_k = 0$ and hence $B_k(K) \subseteq Z_k(K)$. This allows us to define the k th *homology group* of M as

$$H_k(K) := Z_k(K) / B_k(K).$$

We now consider the construction of persistence diagrams. We are given a filtration $K = \{K_r \mid r \in \mathbb{R}\}$ of a countable simplicial complex indexed over the positive real numbers, thought of as time. By this we mean that each K_a is a simplicial complex and that $K_a \subseteq K_b$ for $a < b$. We wish to summarize how the topology of the filtration changes over time. For $a < b$ we have an inclusion map of simplicial complexes $\iota : K_a \rightarrow K_b$. This induces inclusion maps

$$\iota : B_k(K_a) \rightarrow B_k(K_b) \quad \text{and} \quad \iota : Z_k(K_a) \rightarrow Z_k(K_b).$$

This induces homomorphisms (which are generally not inclusions)

$$\iota_k^{a \rightarrow b} : H_k(K_a) \rightarrow H_k(K_b).$$

We can define the persistence homology groups $H_k(a, b)$ by

$$H_k(a, b) := Z_k(K_a) / (Z_k(K_a) \cap B_k(K_b)).$$

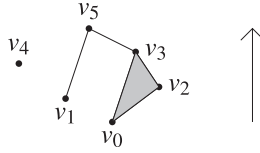
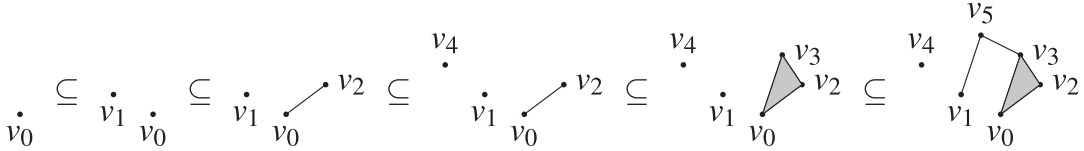
Here, $H_k(a, b)$ is the group of homology classes in $H_k(K_a)$ which persist to $H_k(K_b)$ or in other words the image of $\iota_k^{a \rightarrow b}$.

We say that a homology class $\alpha \in H_k(K_i)$ is *born* at time a (denoted as $\text{b}(\alpha)$) if it is in the cokernel of $\iota_k^{a' \rightarrow a}$ for any $a' < a$. The cokernel of $f : X \rightarrow Y$ is $Y / \text{im } f$. It can be thought of as the vector subspace of Y which is perpendicular to $\text{im } f$. More precisely, we can say an entire coset is born but this can be represented by the element in the vector space perpendicular to $\text{im } f$.

For α born at time a , we say that α *dies* at time b (denoted as $\text{d}(\alpha)$) if, for all $a' < a < b' < b$, we have $\iota_k^{a' \rightarrow b}(\alpha) \in \text{im } \iota_k^{a' \rightarrow b}$ but $\iota_k^{a \rightarrow b'}(\alpha) \notin \text{im } \iota_k^{a \rightarrow b'}$. Informally, we can think of the process of dying as either becoming zero or merging into a pre-existing homology class. For example, suppose we have two connected components, one represented by the H_0 class α_0 and is born at time 0 and the other represented by the H_0 class α_1 and is born at time 1. If these components become connected at time 2, then we say α_1 dies at time 2. We say that α is an *essential class* of K if it never dies. We say the homology class α has *persistence* $\text{d}(\alpha) - \text{b}(\alpha)$.

Let $\mathbb{R}^{2+} := \{(a, b) \in (-\infty \cup \mathbb{R}) \times (\mathbb{R} \cup \infty) : a < b\}$. We define the k th persistence diagram corresponding to the filtration K to be the multiset of points in \mathbb{R}^{2+} alongside countably infinite copies of the diagonal such that the number of points (counting multiplicity) in $[-\infty, a] \times [b, \infty]$ is equal to the dimension of $H_k(a, b)$. That is, it is equal to the dimension of the space of k -dimensional homology

¹ $\text{im}(f) = \{y : f(x) = y \text{ for some } x\}$ is called the image of f and $\ker(f) = \{x : f(x) = 0\}$ is called the kernel of f .

FIG. 2. The simplicial complex K and the vertical height direction.FIG. 3. The filtration of K by height in direction v . Each simplex is included at its maximal height.

classes that are born at or before a and die at or after b . This is achieved by placing at each (a, b) a number of points equal to dimension of the space of k -dimensional homology classes that are born at time a and die at time b . The countably infinite copies of the diagonal play the role of persistent homology classes whose persistence is zero and hence would not otherwise be seen.

We restrict our attention to persistence diagrams such that

$$\sum_{\alpha \text{ not essential}} d(\alpha) - b(\alpha) < \infty.$$

This is automatically true if the persistence diagrams contain finitely many off-diagonal points.

Let us consider an example. Consider the simplicial complex in the plane shown in Fig. 2 and the filtration by sublevel sets of vertical height (as shown by the arrow).

The subcomplex at time t is the set of all simplices that entirely lie at or below height t . This constructs the filtration in Fig. 3. We then can keep track of how the 0th dimensional homology changes as we progress through the filtration.

A component (v_0) is born in the first stage of the filtration at time t_0 . This component corresponds to an essential class that lives throughout the rest of the filtration. It corresponds to a point in the persistence diagram at (t_0, ∞) . At t_1 of the filtration a new component appears (v_1) . It joins the first component at the last stage and so corresponds to a point in the persistence diagram at (t_1, t_5) . Another component appears (v_4) at t_3 . This component is always separate and hence it corresponds to an essential class. It is represented by a point in the persistence diagram at (t_3, ∞) . In this example, there is no homology class of dimensions > 0 , so the higher-dimensional persistence diagrams have no off-diagonal points.

Let \mathcal{D} denote the space of persistence diagrams. There are many choices of metric on \mathcal{D} just as there are many choices of metrics on spaces of functions. The coordinates of the points in the persistence diagrams have special meanings (birth or death times) and hence deserve to be treated (somewhat) individually. A small, localized change in a filtration will often affect only one of the two coordinates.

Let X and Y be persistence diagrams. We can consider bijections ϕ between the points and copies of the diagonal in X and the points and copies of the diagonal in Y . Bijections always exist because there are countably many copies of the diagonal which everything can be paired with. These bijections are

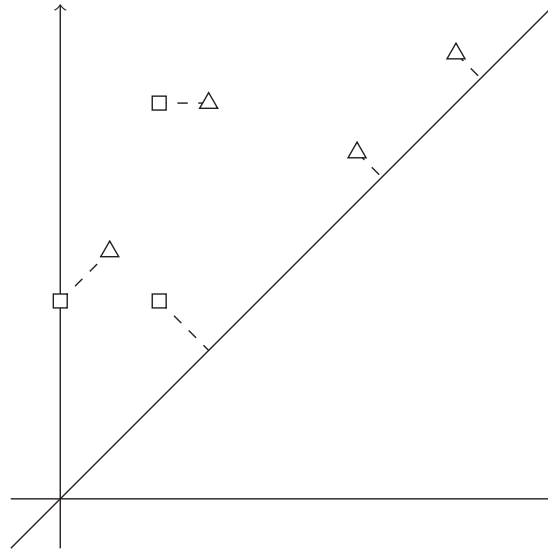


FIG. 4. The dashed lines indicate an optimal bijection from the persistence diagram consisting of the square points (and copies of the diagonal) to the persistence diagrams consisting of the triangle points (and copies of the diagonal).

the transport plans to be considered for the Wasserstein distance. For $p \in [1, \infty)$ define

$$\text{dist}_p(X, Y) = \left(\inf_{\phi: X \rightarrow Y} \sum_{x \in X} \|x - \phi(x)\|_p^p \right)^{1/p}. \quad (2.1)$$

These metrics are analogous to p -Wasserstein distances on the space of measures, or L_p distances on the space of functions on a discrete set. More details about the range of metric choices are discussed in [39, 41].

We call a bijection optimal if it achieves the infimum in (2.1). The existence of an optimal bijection (which is not necessarily unique) is proved in [39]. We illustrate in Fig. 4, an example of the optimal bijection between two persistence diagrams.

We found the $p = 1$ choice (in (2.1)) to perform better than other metrics in empirical studies. We suspect that the variation in performance for different distance metrics is driven by variation in the pairing of points to the diagonal. From now on let $\text{dist}(X, Y)$ denote $\text{dist}_1(X, Y)$.

2.2 Computing the persistence homology transform

Let M be a subset of \mathbb{R}^d which can be written as a finite simplicial complex. For any unit vector $v \in S^{d-1}$, we define a filtration $M(v)$ of M parameterized by a height r where

$$M(v)_r = \{x \in M : x \cdot v \leq r\}$$

is the subcomplex of M containing all the simplices below height r in the direction v . We see that $M(v)_r$ and $\{\Delta \in M : x \cdot v \leq r \text{ for all } x \in \Delta\}$ are homotopy equivalent² and hence their homology groups are the same. The k th dimensional persistence diagram, $X_k(M, v)$, summarizes how the k th dimensional homology of the filtration $M(v)$ changes over the height parameter r . By stability results on persistence diagrams [13, 40], the map $v \mapsto X_k(M, v)$ is Lipschitz.

LEMMA 2.1 The map $v \mapsto X_k(M, v)$ is Lipschitz (and hence also continuous) with respect to the distance metric $\text{dist}(\cdot, \cdot)$ whenever M is a finite simplicial complex.

Proof. Since M is a finite simplicial complex, there is a bound N on the number of off-diagonal points in any diagram $X_k(M, v)$. There also is a bound K on the distance of any point in M to the origin. Consider the functions h_{v_1} and h_{v_2} on M which are the height functions in directions v_1 and v_2 , respectively. That is, for x in M we have $h_{v_i}(x) = x \cdot v_i$. Now

$$|h_{v_1}(x) - h_{v_2}(x)| = |x \cdot v_1 - x \cdot v_2| \leq \|x\|_2 \|v_1 - v_2\|_2 \leq K \|v_1 - v_2\|_2.$$

and hence

$$\|h_{v_1} - h_{v_2}\|_\infty \leq K \|v_1 - v_2\|_2. \quad (2.2)$$

The bottleneck stability theorem tells us that

$$\text{dist}(X_k(M, v_1), X_k(M, v_2)) \leq N \|h_{v_1} - h_{v_2}\|_\infty.$$

Combined with (2.2), we can conclude

$$\text{dist}(X_k(M, v_1), X_k(M, v_2)) \leq NK \|v_1 - v_2\|_2$$

and hence $v \mapsto X_k(M, v)$ is Lipschitz with respect to dist_1 . □

The above lemma generalizes to all $p \geq 1$ for the family of distance metrics (2.1) on \mathcal{D} .

REMARK 2.1 The above lemma generalizes to all $p \geq 1$ for the family of distance metrics (2.1) on \mathcal{D} . In particular, in the case $p = \infty$, the Lipschitz constant is bounded by the distance of the furthest point in M to the origin.

DEFINITION 2.1 The *PHT* of $M \subset \mathbb{R}^d$ is the function

$$\begin{aligned} \text{PHT}(M) : S^{d-1} &\rightarrow \mathcal{D}^d \\ v &\mapsto (X_0(M, v), X_1(M, v), \dots, X_{d-1}(M, v)). \end{aligned}$$

By Lemma 2.1, we know the PHT of a finite simplicial complex is continuous. Let $C(X, Y)$ denote the space of continuous functions from X to Y . We have shown that, for $M \subset \mathbb{R}^d$, if M has a finite simplicial complex representation, then $\text{PHT}(M) \in C(S^{d-1}, \mathcal{D}^d)$.

Let \mathcal{M}_d be the space of subsets of \mathbb{R}^d that can be written as finite simplicial complexes. More precisely, we can think of pairs (K, f) where K is a finite simplicial complex, and $f : K \rightarrow \mathbb{R}^d$ such that the restriction of f to any simplex in K is linear and the preimage under f of every point in the image of K is starlike. Observe that this last condition ensures that $f(K)$ is homotopy equivalent to K .

² Two spaces are ‘homotopy equivalent’ if we can continuously deform (without tearing or glueing) one into the other. Homology is invariant under such continuous changes.

We then define \mathcal{M}_d to be the space of all pairs (K, f) under the equivalence $(K_1, f_1) \sim (K_2, f_2)$ when $f_1(K_1) = f_2(K_2)$.

Our main results concern the injectivity of the PHT.

PROPOSITION The PHT is injective when the domain is \mathcal{M}_d for $d = 2, 3$.

We provide in Section 3, a proof of the above statement. The proof is constructive and provides an algorithm that reconstructs a simplicial complex from the persistence diagrams that compose the PHT of the simplicial complex. The persistence diagrams track features—quantifying where they begin and end from the perspectives of the directions they correspond to. The injectivity proof also shows that the PHT is theoretically invertible.

The PHT can be used to define a distance metric between shapes or surfaces

$$\text{dist}_{\mathcal{M}_d}(M_1, M_2) := \sum_{k=0}^d \int_{S^{d-1}} \text{dist}(X_k(M_1, v), X_k(M_2, v)) \, dv. \quad (2.3)$$

We can show that $\text{dist}_{\mathcal{M}_d}$ is a distance metric on \mathcal{M}_d . The proof of the above proposition requires knowing the persistence diagrams in every direction. However, the stability results Lemma 2.1 reassure that the error in approximating our distance function $\text{dist}_{\mathcal{M}_d}$ using only a finite sampling of directions should be small.

Simplicial complexes that are homeomorphic to a sphere are a class within \mathcal{M}_2 or \mathcal{M}_3 of independent interest. For this class the 0th dimensional persistence diagrams are sufficient to characterize the simplicial complexes. The advantage of this is that the computation of the 0th dimensional homology persistence diagrams is very fast. We can use a union-find algorithm which is (almost) linear in the number of vertices in the simplicial complex. The following fact is discussed further in Section 3.3.

PROPOSITION Given a simplicial complex $M \subset \mathbb{R}^3$ (respectively, \mathbb{R}^2) which is homeomorphic to S^2 or S^1 (respectively, S^1), we can construct $X_k(M, v)$ from $X_0(M, v)$ and $X_0(M, -v)$ for $k = 1, 2$.

The above proposition motivates the following definition of the 0th dimensional PHT.

DEFINITION 2.2 The 0th dimensional PHT of $M \in \mathbb{R}^d$ is the function

$$\begin{aligned} \text{PH}_0\text{T}(M) : S^{d-1} &\rightarrow \mathcal{D} \\ v &\mapsto X_0(M, v). \end{aligned}$$

We now will illustrate an example of the 0th dimensional PHT of a simplicial complex shaped like the letter M in the plane. We have the persistence diagrams generated by height functions in eight different directions illustrated in Fig. 5. This is a crude discretization of the PHT of that particular embedding of the letter M in the plane.

We can define distance metrics for simplicial complexes homeomorphic to the sphere. Define $\mathcal{S}(d, k)$ as the space of simplicial complexes in \mathbb{R}^d homeomorphic to S^k . Proposition 2.2 suggests the following alternative metric for the spaces $\mathcal{S}(2, 1)$, $\mathcal{S}(3, 1)$ and $\mathcal{S}(3, 2)$:

$$\text{dist}_{\mathcal{S}(d, k)}(M_1, M_2) := \int_{S^{d-1}} \text{dist}(X_0(M_1, v), X_0(M_2, v)) \, dv.$$

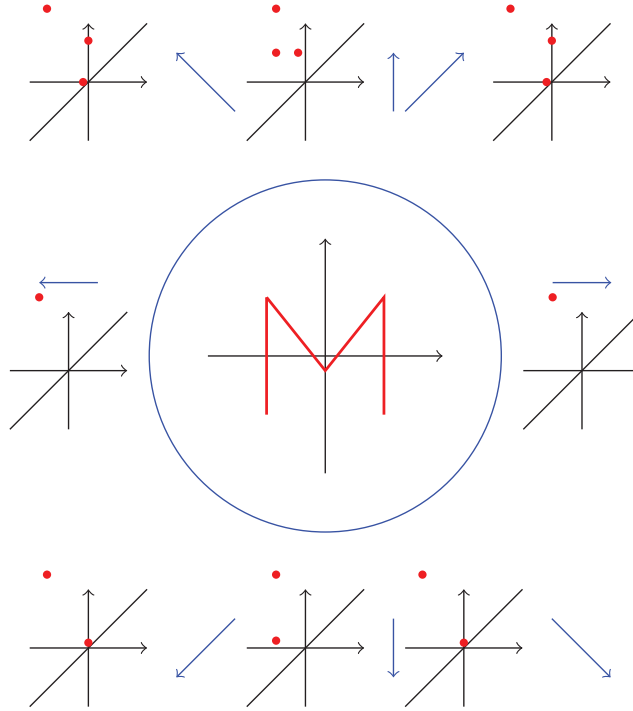


FIG. 5. The 0th dimensional persistence diagrams corresponding to filtrations of the letter M by height functions of eight different directions. The points with ∞ in the second coordinate are represented by a point with second coordinate just above the axes.

3. Injectivity of the transform

We prove that the PHT is an injective map. It will also imply a method for the alignment of shapes, which is computationally feasible only in \mathbb{R}^2 . In the final subsection, we discuss a slight variant of the PHT which we call the Euler (characteristic) curve transform (ECT).

3.1 Injectivity

THEOREM 3.1 The PHT is injective when the domain is \mathcal{M}_3 .

Proof. The proof is constructive. We state the proof as an algorithm. Given a function $\text{PHT}(M) : S^2 \rightarrow \mathcal{D}^3$, we state a procedure to find all the vertices in one of the simplest representations of the simplicial complex. By simplest we mean a representation as a simplicial complex with the fewest possible number of vertices. We then determine the link of each vertex. Since M is assumed to be piecewise linear, computing the vertices and links is enough for reconstruction.

We first provide some facts that we will use in the procedures to reconstruct M from $\text{PHT}(M)$:

- (1) Changes in homology of sublevel sets of height functions in any direction can only occur at the heights of vertices of M .

- (2) Every vertex x determines a critical point for an open ball in the set of all directions (recall that the set of all directions is S^2). That is to say that the inclusion of this point x causes a birth or a death of a homology class. The homology class is also consistent inside the ball. We claim that there is some ball of $\{v\} \subset S^2$ with points (a_v, b_v) in the corresponding diagrams that continuously change with either $a_v = x \cdot v$ or $b_v = x \cdot v$.

We will prove these claims later in this proof.

We first define some maps that we will use. Fix a vertex x of M , and a direction $v \in S^2$. Let $M(v)_{x \cdot v}$ be the sublevel set of h_v from the height $h_v(x)$ and let $M(v)_{x \cdot v}^-$ be the sublevel set of h_v from the height $h_v(x) - \delta$ where $\delta > 0$ is sufficiently small enough that no critical values of h_v occur in $(h_v(x) - \delta, h_v(x))$. The finiteness assumption on the simplicial complex ensures that a suitable $\delta > 0$ exists. By the definition of relative homology we have the following exact sequence:

$$\begin{aligned} \cdots \rightarrow H_i(M(v)_{x \cdot v}^-) \xrightarrow{\iota_*} H_i(M(v)_{x \cdot v}) \rightarrow H_i(M(v)_{x \cdot v}, M(v)_{x \cdot v}^-) \\ \xrightarrow{\iota_*} H_{i-1}(M(v)_{x \cdot v}^-) \rightarrow H_{i-1}(M(v)_{x \cdot v}) \rightarrow \cdots \end{aligned}$$

where ι_* is the map on homology induced by the inclusion map. The above implies

$$\begin{aligned} H_i(M(v)_{x \cdot v}, M(v)_{x \cdot v}^-) &= 0 \text{ for } i \geq 3 \\ H_0(M(v)_{x \cdot v}, M(v)_{x \cdot v}^-) &\simeq \text{coker}\{H_0(M(v)_{x \cdot v}^-) \rightarrow H_0(M(v)_{x \cdot v})\} \\ H_2(M(v)_{x \cdot v}, M(v)_{x \cdot v}^-) &\simeq \text{coker}\{H_2(M(v)_{x \cdot v}^-) \rightarrow H_2(M(v)_{x \cdot v})\} \\ &\quad \oplus \ker\{H_1(M(v)_{x \cdot v}^-) \rightarrow H_1(M(v)_{x \cdot v})\} \\ H_1(M(v)_{x \cdot v}, M(v)_{x \cdot v}^-) &\simeq \text{coker}\{H_1(M(v)_{x \cdot v}^-) \rightarrow H_1(M(v)_{x \cdot v})\} \\ &\quad \oplus \ker\{H_0(M(v)_{x \cdot v}^-) \rightarrow H_0(M(v)_{x \cdot v})\}. \end{aligned} \tag{3.1}$$

The ranks of the above kernels and cokernels can be read from the appropriate persistence diagrams. Let $\tilde{\beta}_i(x, v) := \text{rank}(H_i(M(v)_{x \cdot v}, M(v)_{x \cdot v}^-))$ denote the relative homology Betti numbers.³ We can compute these relative homology Betti numbers using (3.1). We have $\tilde{\beta}_i(x, v) = 0$ for $i \geq 3$. We have $\tilde{\beta}_2(x, v)$ is the number of classes in $X_2(M, v)$ that are born at height $h_v(x)$ plus the number of classes in $X_1(M, v)$ that die at height $h_v(x)$. Similarly $\tilde{\beta}_1(x, v)$ are the number of classes in $X_1(M, v)$ that are born at height $h_v(x)$ plus the number of classes in $X_0(M, v)$ that die at height $h_v(x)$. Finally, $\tilde{\beta}_0(x, v)$ is the number of classes in $X_0(M, v)$ that are born at height $h_v(x)$. We will infer the link of x by considering how these ranks vary across $v \in S^2$.

We now prove claim (1): that changes in homology can only happen when a height function reaches a vertex. This is because if x is not a vertex, then, for a sufficiently small $\delta > 0$, we have $H_k(M(v)_{x \cdot v}, M(v)_{x \cdot v}^-) = 0$ for all k and all directions v . This lack of homology is reflected in a corresponding lack of points in the persistence diagrams.

The proof of claim (2) will become apparent later. It is clear that if x is an isolated vertex, then an H_0 class is born at height x_i in every direction, so we will only need to later prove this claim for vertices that are not isolated.

³ Under nice circumstances (which are always true in this paper's setting) the relative homology groups $H_*(A, B)$ are the same as the reduced homology groups $\tilde{H}_*(A/B)$ where A/B is the set of points in A after we glue all of B together into a single point. Relative homology is almost the same as normal homology except we reduce the dimension by one when looking at the 0th dimensional reduced homology. This implies that $\tilde{\beta}_k(K) = \beta_k(K)$ for $k > 0$ and $\tilde{\beta}_0(K) = \beta_0(K) - 1$.

Finding vertices: We now provide a procedure to find the vertices given the above claims. Both coordinates (when finite) of every point in every persistence diagram must be accounted for. This is how we can guarantee that all of the vertices have been found. We follow this algorithm repeatedly:

- (1) Choose a direction v , a dimension k and a point $(a_v, b_v) \in X_k(M, v)$
- (2) The continuity of $X_k(M, v)$ as v varies ensures that there is a radius $r > 0$ such that there is a well-defined and continuous set of points (a_u, b_u) for each $u \in B(v, r)$ including the point (a_v, b_v) .
- (3) Consider $0 < r' < r$. If there exists a point $x \in \mathbb{R}^3$ such that $a_u = x \cdot u$ for all $u \in B(v, r')$, then x is a vertex in M . We now have accounted for a_u for $u \in B(v, r')$.
- (4) Consider $0 < r' < r$. If there exists a point $x \in \mathbb{R}^3$ such that $b_u = x \cdot u$ for all $u \in B(v, r')$, then x is a vertex in M . We now have accounted for b_u for $u \in B(v, r')$.

This procedure will find all the vertices in the simplicial complex.

Finding links: Given the set of vertices $\{x_i\}_{i=1}^n$, we need to find the link structure for each vertex to complete the proof. Fix a vertex x . The link of the vertex x is $\partial B(x, r) \cap M$ for a suitable small $r > 0$, and then scaled to the unit sphere. Denote the link of x as $L(x)$.

If a vertex x is isolated (i.e. has an empty link), then an H_0 class is born at height $x \cdot v$ in every direction v and this point results in no other changes in homology. This can be read off the persistence homology transform. From now on suppose that x is not isolated.

We first will wish to find the ‘essential’ edges out of x . We can consider an edge to be essential if every simplicial representation of M with vertices $\{x_i\}_{i=1}^n$ must contain that edge. For example, the sides of a rectangle are essential but the diagonals are not. For each essential edge out of x we will determine in what directions perpendicular to that edge M exists. From this information, using the piecewise linear structure of M , we can piece together the link at x .

From now on we will only be considering essential edges and all mention of edges will mean essential edges. We can observe that if M is a simplicial complex whose vertices are in general position, then every edge is essential.

Recall that $\tilde{\beta}_k(x, v) = \text{rank}(H_k(M(v)_{x \cdot v}, M(v)_{x \cdot v}^-))$. Let

$$\tilde{\chi}(x, v) := \tilde{\beta}_0(x, v) - \tilde{\beta}_1(x, v) + \tilde{\beta}_2(x, v).$$

This is the change in the Euler characteristic from $M(v)_{x \cdot v}^-$ to $M(v)_{x \cdot v}$. Suppose that e is an edge out of x . Without loss of generality, we orient S^2 (the range of directions in which we consider the corresponding height functions) to have e pointing to the north pole. If e is isolated (i.e. its link is empty), then it contributes a path from x to $M(v)_{x \cdot v}^-$ whenever v is in the southern hemisphere which is not available for any direction in the northern hemisphere. This means that there is a contribution of increasing $\tilde{\beta}_1(x, v) - \tilde{\beta}_0(x, v)$ (and hence decreasing $\tilde{\chi}(x, v)$) by 1 as v passes southwards across the equator. This contribution is illustrated in Fig. 6.

Suppose now that the edge e is not isolated. We need to further consider its link. More precisely, we will consider the range of directions perpendicular to e within M . Consider the great circle perpendicular to e which is now the equator due to our orientation. Project onto the ball the directions that emanate perpendicularly from e . Taking a bird’s eye view, we can split the equator into regions depending on how many components are in this projection of the link of e intersected with the other half of this equator. This is illustrated in Fig. 7.

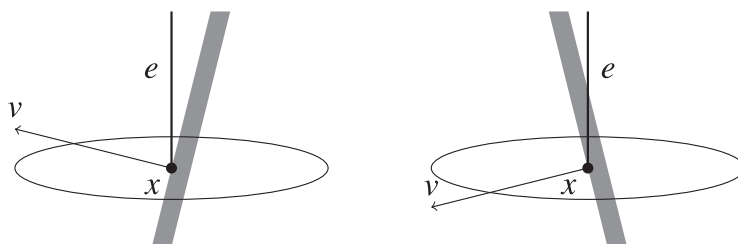


FIG. 6. As v changes from the northern to the southern hemisphere the edge e becomes included in $(M(v)_{x,v}, M(v)_{x,v}^-)$, which here is indicated by the gray shaded region. The edge e acts as an extra path from x to $M(v)_{x,v}^-$ which increases $\tilde{\beta}_1(x, v) - \tilde{\beta}_0(x, v)$.

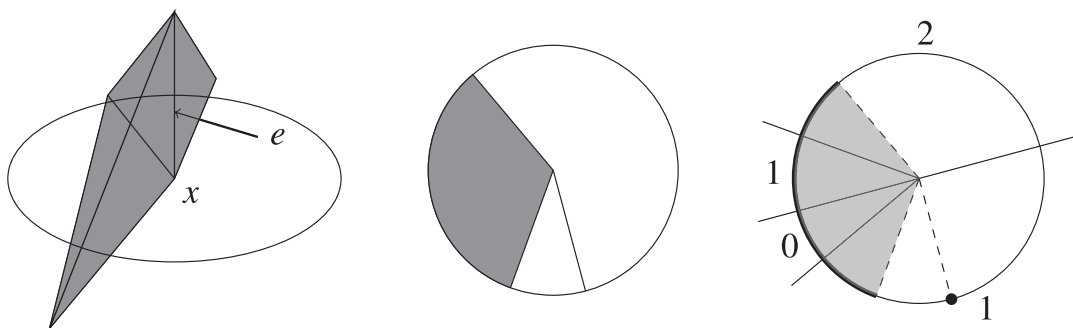


FIG. 7. The simplicial complex near e , then taking a bird's eye view down e , and finally the number of components appearing in the alternate semicircle to that vector over regions of the circle.

We are interested in how the $\tilde{\chi}(x, v)$ changes as v passes the equator traveling south. There are the following possibilities:

- (0) If there are no components, then a new set of paths from x to $M(v)_{x,v}^-$ is born and the $\tilde{\beta}_1(x, v) - \tilde{\beta}_0(x, v)$ is increased by 1 as v passes southwards. (This is comparable with the isolated edge case as we do not 'see' any part of the link of e and is illustrated in Fig. 6.)
- (1) If there is one component, then there is no change to any of the $\tilde{\beta}_i(x, v)$ as v passes southwards.
- (2) If there are 2, then $\tilde{\beta}_2(x, v) - \tilde{\beta}_1(x, v)$ is increased by 1 as v passes southwards. Either $\tilde{\beta}_2(x, v)$ is increased as two already connected components (connected outside of the link of the edge) join or $\tilde{\beta}_1(x, v)$ is decreased as two formerly unconnected components. Examples of this are illustrated in Figs 8 and 9.
- (k) If there are k components, $k > 1$, then $\tilde{\beta}_2(x, v) - \tilde{\beta}_1(x, v)$ is increased by $k - 1$ as v passes southwards. The idea is a generalization of the two-component case. We can construct a graph G with one vertex for each of the connected components in Fig. 7. We add edges between these 'connected component' vertices when there is some face in M (with x in its boundary) between them. When v lies below the equator $M(v)_{x,v}/M(v)_{x,v}^-$ is homotopy equivalent to double cone on G . For v lying above the equator, we create a different graph G' which is the same as G but we add a vertex representing the edge e and also add k edges, one for each of the connected components. These edges go from the vertex representing e to the vertex representing

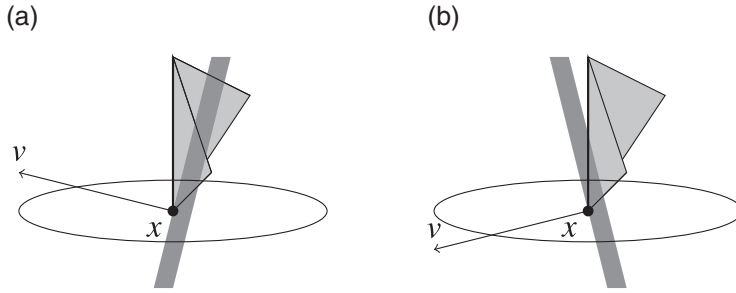


FIG. 8. In (a), when v is above the equator, $M(v)_{x,v}/M(v)_{x,v}^-$ is homotopy equivalent to circle. The addition of x into the sublevel sets creates a loop. In (b), when v is below the equator, $M(v)_{x,v}/M(v)_{x,v}^-$ is homotopy equivalent to a point. The inclusion of x is a continuous variation and hence does not change the homology. As v passes the equator southwards we switch between these cases and $\tilde{\beta}_1(x, v)$ decreases by one.

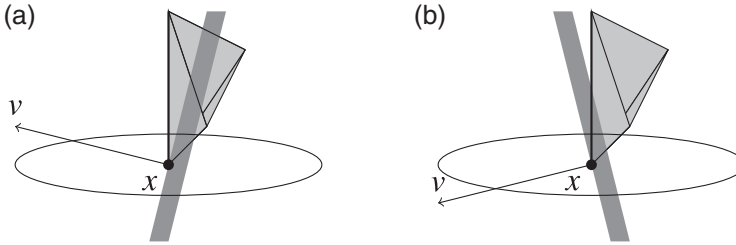


FIG. 9. In (a), when v is above the equator, $M(v)_{x,v}/M(v)_{x,v}^-$ is homotopy equivalent to point. The addition of x into the sublevel sets is a continuous variation and hence does not change the homology. In (b), when v is below the equator, $M(v)_{x,v}/M(v)_{x,v}^-$ is homotopy equivalent to a 2-sphere. The inclusion of x into the sublevel sets completes the outside of a void. As v passes the equator southwards we switch between these cases and $\tilde{\beta}_2(x, v)$ increases by one.

the corresponding connected component. For v lying below the equator, $M(v)_{x,v}/M(v)_{x,v}^-$ is homotopy equivalent to the double cone on G' . As v passes, southwards we effectively glue one edge and k disks to get from the double cone on G to the double cone on G' . This increases $\tilde{\beta}_2(x, v) - \tilde{\beta}_1(x, v)$ is by $k - 1$. For example, in the case of $k = 2$, we have two possible graphs for G ; either two disconnected vertices (as shown in Fig. 8) or two vertices connected by one edge (as shown in Fig. 9).

Together we see that the link at e causes $\tilde{\chi}(x, v)$ to increase by $k - 1$ if the link of e intersected with the semicircle furthest from v contains k components. For each edge e , let f_e denote the function on the great circle perpendicular to e of the changes in $\tilde{\chi}(x, v)$ as we pass ‘southwards’ over the equator away from e . Knowing the function f_e is equivalent to knowing, at each location, how many components lie in the alternate semicircle. This in turn is equivalent to knowing the birds eye picture as illustrated in Fig. 7, which is in turn equivalent to knowing the link of e .

We cannot make any comments about what happens on the equator itself. However, there are only finitely many vertices and so there are only finitely many edges. In turn this implies that the set of directions perpendicular to an edge at x is of measure zero. From now on we only consider functions up to sets of measure zero.

The sphere of directions can be partitioned into regions bounded by finitely many great circles perpendicular to edges emanating from x . Within the same region the $\tilde{\chi}$ remains constant. The above process shows how $\tilde{\chi}$ varies as it passes between regions. Consider an edge e . From our assumption that we are considering an essential edge we know that the number of components is not 1 for some open interval along the great circle perpendicular to e . This implies that at least one region bounded by great circles has non-zero $\tilde{\chi}$ and hence x determines a critical point for directions in that region. This proves claim (2).

We now describe how we scan all the vertices and find their links:

- (1) Select a direction v_0 for which no vertices have the same height in that direction. We will iterate the following procedure through all the vertices in the order of their height in the direction of v_0 . This is possible as we are only considering simplicial complexes with finitely many vertices. We will scan through the vertices in this direction, building up the complex as new vertices are included. It is useful that at each stage, when we want to find the link of a new vertex, that we already know its neighborhood intersected with the half-plane in the direction $-v_0$. For the base case, we know that we first hit the simplicial complex at some finite time, due to the finiteness condition. The neighborhood of this first vertex x intersected with $M(x, v_0)$ is only the point x itself.
- (2) We now investigate vertex x . We know the sublevel set $M(x, v_0)$. Consider the partition of the sphere around x into regions with the same relative homology. There is a possibility that there are edges e and e' out of x directly opposite to each other with links such that the effects of these links passing over the equator cancel. We can remedy this situation by including in our list of great circles those perpendicular to edges next to x lying in $M(x, v_0)$. This partition tells us which great circles corresponding to edges exist.
- (3) Consider a great circle C found in (2). It has perpendicular normals η and $-\eta$ with $v_0 \cdot \eta < 0$. From $v_0 \cdot \eta < 0$, we know that if there was an edge in the direction of η , then it would be in $M(x, v_0)$. Furthermore, we would know its link.
- (3a) If there is no edge in the direction of η , then there must be an edge e in the direction of $-\eta$. We also know that $f_e = -f$. The minus sign is because of switching the orientation so that e is pointing to the north pole instead of the south. Since we know f_e , we can determine the link of e .
- (3b) If there is an edge e' in the direction of η consider the new function $g = f - f_{e'}$. If g is the zero function (recall everything is up to sets of measure zero), then every change of $\tilde{\chi}$ as vector pass the great circle C can be attributable to e' and hence there is no edge in the direction $-\eta$. If g is not the zero function, then there is an edge e in the direction of $-\eta$. As in the case of (3a), we know that $f_e = -g$ and we can thus determine the link of e .
- (4) For each vertex, in the order outline in (1), we first find the appropriate great circles by step (2). We then iterate step (3) through all great circles. Remember each iteration will assign changes to vertices and/or links and, at the next iteration we ignore previously labeled vertices and links. When we have assigned all the changes, we will have revealed the entire simplicial complex, all the links and vertices. \square

In the theorem and the proof we presuppose that we know $\text{PHT}(M)(v)$ for all $v \in S^2$. But the constructive method of the proof suggests that we could use a supervised learning approach using only

finitely many directions. Unfortunately, this could only give an approximation of the original M up to some error. This is because some vertices may only be ‘seen’ from an arbitrarily small ball of directions which may never be checked.

Although it is possible to write a direct proof for the injectivity of the PHT for simplicial complexes in the plane it is easier and faster to consider it a corollary of the three-dimensional case.

COROLLARY 3.1 The PHT is injective when the domain is \mathcal{M}_2 .

Proof. Let us consider \mathbb{R}^2 as being inside \mathbb{R}^3 with the third coordinate set to zero. This means that we can think of \mathcal{M}_2 as lying inside \mathcal{M}_3 . Consider $M \in \mathcal{M}_2$ as a simplicial complex in \mathbb{R}^3 . Let $v = (v_1, v_2, v_3)$ be a unit vector in \mathbb{R}^3 with $v_3 \neq \pm 1$. Let $(\tilde{v}_1, \tilde{v}_2)$ be the unit vector in the direction of (v_1, v_2) . We have $\tilde{v}_i \|(v_1, v_2)\| = v_i$. Now $M((v_1, v_2, v_3))_r$ is the set of all points (x, y, z) in M (viewed as a subset of \mathbb{R}^3) such that $(x, y, z) \cdot (v_1, v_2, v_3) \leq r$. Now $(x, y, z) \in M$ implies that $z = 0$ and hence $M((v_1, v_2, v_3))_r$ is the set of (x, y) in M (viewed as a subset of \mathbb{R}^2) such that $(x, y) \cdot (v_1, v_2) \leq r$. Now $(x, y) \cdot (v_1, v_2) \leq r$ is equivalent to $(x, y) \cdot (\tilde{v}_1, \tilde{v}_2) \leq r / \|(v_1, v_2)\|$, so we can see that $M((v_1, v_2, v_3))_r$ is in fact $M((\tilde{v}_1, \tilde{v}_2))_{r/\|(v_1, v_2)\|}$. This implies that we can construct $X_p(M, (v_1, v_2, v_3))$ from $X_p(M, (\tilde{v}_1, \tilde{v}_2))$ by appropriately scaling the points in the persistence diagram.

If $v = (0, 0, \pm 1)$, then $M(v)_r$ is empty for $r < 0$ and is M for $r \geq 0$. This tells us that the persistence diagrams simply contain a set of points at $(0, \infty)$ to represent the homology of M .

Finally, note that $X_3(M, v)$ is the empty diagram for all directions $v \in S^2$.

Let $M_1, M_2 \in \mathcal{M}_2$. If $\text{PHT}(M_1) : S^1 \rightarrow \mathcal{D}^2$, is the same as $\text{PHT}(M_2) : S^1 \rightarrow \mathcal{D}^2$ then our above construction process shows that $\text{PHT}(M_1) : S^2 \rightarrow \mathcal{D}^3$ is the same as $\text{PHT}(M_2) : S^2 \rightarrow \mathcal{D}^3$ when both M_1 and M_2 are embedded in \mathbb{R}^3 by setting the third coordinate to be zero. Now the PHT is injective on \mathcal{M}_3 by Theorem 3.1. This implies that $M_1 = M_2$. \square

A result of the above theorem and corollary is that we can model the space of piecewise linear simplicial complexes in \mathbb{R}^3 (or \mathbb{R}^2) by modeling the images of their PHTs which lie inside $C(S^2, \mathcal{D}^3)$ (or $C(S^1, \mathcal{D}^2)$, respectively). We can define distances between two shapes M and M' by the distance between $\text{PHT}(M)$ and $\text{PHT}(M')$ —we can pull back the metric on the space of diagrams to a metric on the space of piecewise linear objects in \mathbb{R}^3 (or \mathbb{R}^2 , respectively).

We could potentially also specify a likelihood over shapes, which is difficult, by defining a likelihood of a collection of points in $C(S^2, \mathcal{D}^3)$, which may be easier. We could use point processes for a likelihood model over PHT space.

3.2 Euler characteristic curve transform

There is a variation of the PHT that is an injective map and has a simple inner product structure. Given the previous height function

$$M(v)_r = \{\Delta \in M : x \cdot v \leq r \text{ for all } x \in \Delta\},$$

the Euler characteristic curve $\chi(M, v)$ is the following function of the Euler characteristic for the subcomplex at values r , $\chi(M, v)(r) = \chi(M(v)_r)$. The Euler characteristic of a subcomplex, which in our case is a surface of a polyhedra, has a simple form

$$\chi(M(v)_r) = V - E + F,$$

where V, E and F are the number of vertices, edges and faces, respectively, of the subcomplex $M(v)_r$. Based on the Euler characteristic and height functions, we can define the Euler (characteristic) curve

transform (ECT) for shapes and surfaces

$$\begin{aligned} \text{ECT}(M) : S^{d-1} &\rightarrow \mathbb{Z}^{\mathbb{R}} \\ v &\mapsto (\chi(M, v)). \end{aligned}$$

A direct consequence of the proof of Theorem 3.1 is that the Euler curve transform (ECT) is also injective.

3.3 Surfaces homeomorphic to spheres

We often have further structure for the set of simplicial complexes of interest, such as they are homeomorphic to a sphere. A common example is the surface of a solid contractible object—e.g. the boundaries of many physical objects. In Section 4, we examine the calcaneus or heel bone of various species. The boundaries of these bones are homeomorphic to S^2 .

COROLLARY 3.2 Let $\mathcal{S}(d, k)$ be the space of piecewise linear surfaces in \mathbb{R}^d that are homeomorphic to S^k . The 0th dimensional PHT is injective when the domain is either $\mathcal{S}(3, 2)$ or $\mathcal{S}(3, 1)$ or $\mathcal{S}(2, 1)$.

Proof. Let us first consider the cases where the domain is either $\mathcal{S}(3, 1)$ or $\mathcal{S}(2, 1)$. It is sufficient to show that, from $\text{PH}_0\text{T}(M)$, we can deduce the persistence diagrams of dimensions 1 as all higher-dimensional homology classes are always zero. Pick a direction v . Since M is homeomorphic to a sphere, the only H_1 class is born exactly when the entire loop is revealed. This is the time that the loop is first hit from the direction $-v$. Since we know the 0th dimensional persistence classes for direction v , we know at what height this is.

Let us now consider the case where the domain is $\mathcal{S}(3, 2)$. It is sufficient to show that, from $\text{PH}_0\text{T}(M)$, we can deduce the persistence diagrams of dimensions 1 and 2. Pick a direction v . We know the 0-dimensional persistence classes by assumption. Since M is homeomorphic to a sphere, the only H_2 class is born exactly when the entire surface is revealed. This is the time that the surface is first hit from the direction $-v$. Since we know the 0th dimensional persistence classes for direction v , we know at what height this is.

To find the H_1 persistent homology classes, we will use Alexander duality. We will need to use persistent cohomology, which is very similar to persistent homology but the induced maps on cohomology go in the opposite direction. The important fact we will use is that persistent homology and persistent cohomology of the same filtration result in the same persistence diagram [15].

Now M by assumption is (homeomorphic to) a sphere and $M(v)_h$ is a compact, locally contractible subset of the M . By Alexander duality $H_1(M(v)_h)$ is isomorphic to $\tilde{H}^0(M(v)_h^c)$ where \tilde{H}^* is reduced cohomology and A^c denotes the complement of A in M . The reduced homology means that we ignore the essential H^0 persistence class. Now $M(v)_h^c$ is homotopy equivalent to $M(-v)_{-h-\epsilon}^-$ for sufficiently small ϵ . These isomorphisms are compatible with the induced maps from inclusions. For $h_1 \leq h_2$, we have the following commutative diagram where the vertical homomorphisms are the homomorphisms induced by inclusion:

$$\begin{array}{ccc} H_1(M(v)_{h_1}) & \xrightarrow{\sim} & \tilde{H}^0(M(v)_{h_1}^c) = \tilde{H}^0(M(-v)_{-h_1}^-) \\ \downarrow & & \downarrow \\ H_1(M(v)_{h_2}) & \xrightarrow{\sim} & \tilde{H}^0(M(v)_{h_2}^c) = \tilde{H}^0(M(-v)_{-h_2}^-) \end{array}$$

This implies that every H_1 persistent homology class for direction v that is born at a and dies at b gets sent under these isomorphisms to an H^0 persistent homology class for direction $-v$ that is born at $-b$ and dies at $-a$. Since the persistence diagrams computed by cohomology and homology are the same, we can compute the H_1 persistence diagrams by flipping the persistence diagrams for H_0 without the essential class. \square

3.4 Unaligned objects and shape statistics

A classic framework for modeling shapes and surfaces is that of shape statistics [7,24,25] where a set of k locations or landmarks on a d -dimensional object (typically considered a manifold) are fixed with $k > d$ and the data consist of the points at these k landmarks, a k -ad [5]. A central idea in shape statistics [7,24,25] is that k -ads should be compared modulo a group of transformations given by how the data are generated. Typically, these transformations are size scaling, rotation and translation.

We now describe how we can adapt our methodology to account for invariance with respect to scaling, translation and rotation. We are given n objects $\{M_1, \dots, M_n\}$, either all in \mathbb{R}^2 or all in \mathbb{R}^3 , and we proceed in three steps: (1) we center the objects; (2) we scale the objects; (3) for each pair of objects we consider all the distances under different rotations and take the smallest of these distances.

Centering: Fix a set of equally spaced directions $\{v_i\}$ (or approximately evenly spaced in for objects in \mathbb{R}^3). We will first give a procedure to center an object at the origin with respect to these directions. We are effectively centering the convex hull of the object. For each direction set λ_i as the time the first component on the shape is seen in direction v_i —that is λ_i is the smallest x such that $(x, \infty) \in X_0(M, v_i)$. Let λ_i^u denote the scalar when the origin is at u . (This is the same as the value obtained by taking the vectors at the normal origin and shifting M by u giving $M - u = \{x - u : x \in M\}$.) The v_i are unit vectors and λ_i^u are signed perpendicular distances to the same hyperplane which has normal v_i . The sign is negative if u is on the v_i side of the hyperplane and is positive if u is on the $-v_i$ side of the hyperplane.

Consider two different potential centers u and w . Considering the λ_i as signed distances implies that $\lambda_i^u - \lambda_i^w = (w - u) \cdot v_i$ and hence

$$\sum_i \lambda_i^u v_i - \sum_i \lambda_i^w v_i = \sum_i (\lambda_i^u - \lambda_i^w) v_i = \sum_i [(w - u) \cdot v_i] v_i = K(w - u). \quad (3.2)$$

where K is a constant independent of w and u so long as the v_i are symmetric with respect to some basis set of vectors. This K can be easily computed given the specific set of directions of v .

We will define the center to be the point u such that $\sum_i \lambda_i^u v_i = 0$. Equation (3.2) shows that this is unique and that this center is computed (starting with w as the origin) by $u = (1/K) \sum_i \lambda_i v_i$

We center M by shifting it by u

$$\tilde{M} = M - u = \{x - u : x \in M\}.$$

The PHT of \tilde{M} is related to that of M in that, for each persistent homology class at $(a, b) \in X_p(M, v)$, we have the same persistent homology class at $(a - u \cdot v, b - u \cdot v) \in X_p(\tilde{M}, v)$. For simplicity of notation we rename the centered object M , $M \leftarrow \tilde{M}$. We apply this procedure to each object.

Scaling: Set an arbitrary scale parameter C , e.g. $C = 1$. Compute $L = -\sum_i \lambda_i > 0$ —these are the same $\{\lambda_i\}$ used in the centering procedure. We now rescale $M \leftarrow (C/L)M = \{(C/L)x : x \in M\}$ for the scaled object $\sum_i \lambda_i = C$. This is done for each object.

Rotating: For each pair M_j, M_k of centered and scaled objects we now consider the different distances under different rotations. We set a subgroup in the group of rotations $\{R_i\}_{i=1}^G$. Set the unaligned distance

between M_j and M_k to be

$$\inf_{i=1,\dots,G} \text{dist}_{\mathcal{M}_d}(M_j, R_i(M_k)).$$

This unaligned distance gives a metric on unaligned objects in \mathbb{R}^d

In the case of objects in \mathbb{R}^2 we can take the $\{v_i\}$ to be evenly spaced unit vectors. The set of rotations can be $\{R_k : R_k v_i = v_{k+i}\}$. In this case, we do not need to compute any more persistence diagrams—we just relabel the ones that have already been computed.

In Section 4.2.1, we will be applying the above procedure to the bounding circles of a set of silhouette images in the plane.

4. Results real and simulated data

To illustrate the utility of the PHT, we look at two related problems, computing the pairwise distance between a set of aligned objects, and comparing unaligned objects. Before stating results on a data set of shapes and real data consisting of bones, we first state the algorithm used to compute distances between objects.

4.1 Distance algorithm

To compute the PHT of an object, we need to compute the persistence diagrams of the height function from various directions. For purposes of computation, we will use a finite set of vectors sampled from S^{d-1} and average the distance between diagrams of two objects; this serves a numerical approximation of the distance defined in (2.3).

Let O_1, \dots, O_N be the objects we wish to compare. Let v_1, v_2, \dots, v_K be the normal vectors we use. Let f_{ik} be the height function on O_i in the direction v_k . Let $X(f_{ik})$ be the persistence diagram constructed using sublevel sets of f_{ik} . The following pseudocode states the algorithm that computes distances:

Distance computation algorithm

Data: Objects O_1, \dots, O_N , K directions v_1, \dots, v_K

Results: Pairwise distances

initialization—all pairwise distances $d_{ij} = d(O_i, O_j)$ set to 0;

For $i = 1$ to N

 For $k = 1$ to K

 Compute $X(f_{ik})$;

For $i = 1$ to N ;

 For $j \leq i$

 For $k = 1$ to K

$d_{ij}^+ = d(X(f_{ik}), X(f_{jk}))$;

$d_{ij} = \frac{d_{ij}^+}{K}$.

We need a set of directions v_1, v_2, \dots, v_K in the above algorithm. For $d = 2$ (that is, shapes in the plane) we used 64 evenly spaced directions. For $d = 3$ (that is simplicial complexes in \mathbb{R}^3) we used 162 directions from S^2 based on a grid constructed by subdividing an icosahedron. For 0-dimensional persistence, we use the union-find algorithm for efficiency. The amortized time per operation for the union-find algorithm is $O(\alpha(n))$, where $\alpha(n)$ is the inverse of the Ackermann function $A(n, n)$, which grows extremely quickly. For any reasonable n , $\alpha(n)$ is < 5 . Thus, the amortized running time per operation

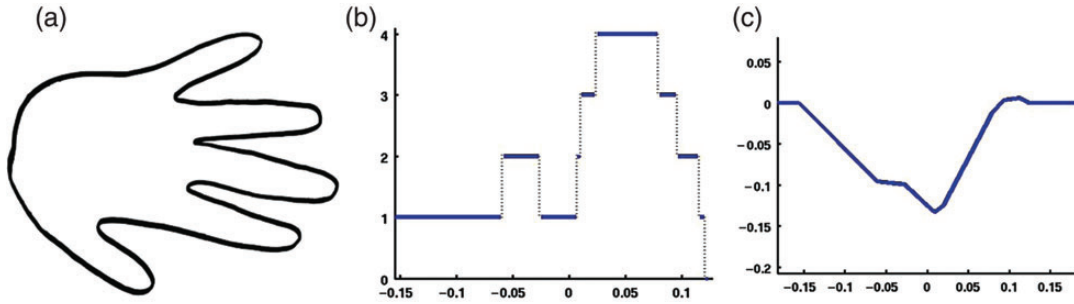


FIG. 10. (a) A 2D contour of a hand, (b) EC curve of the 2D contour of a hand and (c) the associated (centered) cumulative EC curve.

is effectively a small constant. Thus, in each direction, computing the persistence diagram $X_0(M, v)$ is effectively linear in the number of vertices in the simplicial complex.

For each pair of objects, we use the Hungarian algorithm to compute the distances between two persistence diagrams in each of the directions. The runtime complexity of the Hungarian algorithm is $O(m^3)$, where m is the number of off-diagonal points in the two diagrams X and Y combined.

4.2 Results on data sets

We have used the metric on the space of PHTs to analyze a variety of data sets. In Appendix, we consider ellipsoids and hyperboloids with restricted z values. In these examples, we have used the algebraic structure to compute and describe what the PHTs are. We also analyze the resulting distance matrices using multidimensional scaling and give a geometrical interpretation of the coordinates. In this section, we present the results when applying the PHT to both a shape database (of contractible shapes in the plane) and to a data set of pre-aligned calcanei of primates.

4.2.1 Results on a shape database. To examine how well we could measure distances between planar shapes and how well our method can align shapes with respect to scaling, translation and rotation, we studied the performance on a standard shape data set. A shape database that has been commonly used in image retrieval is the MPEG-7 shape silhouette database [36]. We used a subset of this database [28] which includes seven class of objects: Bone, Heart, Glass, Fountain, Key, Fork and Axe. There were 20 examples for each class for a total of 1400 shapes. The shapes are displayed in Fig. 10.

We used the perimeters of the silhouettes which are available at [22]. We applied the alignment algorithm we stated in Section 3.4 to shift and scale the silhouettes. These perimeters are all homeomorphic to a circle so we used the 0th dimensional PHT with 64 evenly spaced directions. We computed the distances between all objects—pairwisely checking under different rotations and taking the minimum as outlined in Section 3.4. We then used multidimensional scaling [27] on the computed distance matrix to project the data into two or three dimensions. In Fig. 11, we see that except for the Axe and Fork classes the objects are separated.

4.2.2 Results on real data—calcanei of primates Information on the pattern of change in anatomical form and diversity of form through time comprises evidence fundamental to hypotheses in evolutionary biology. Often there is great interest in relating the genetic variation in species with variation in

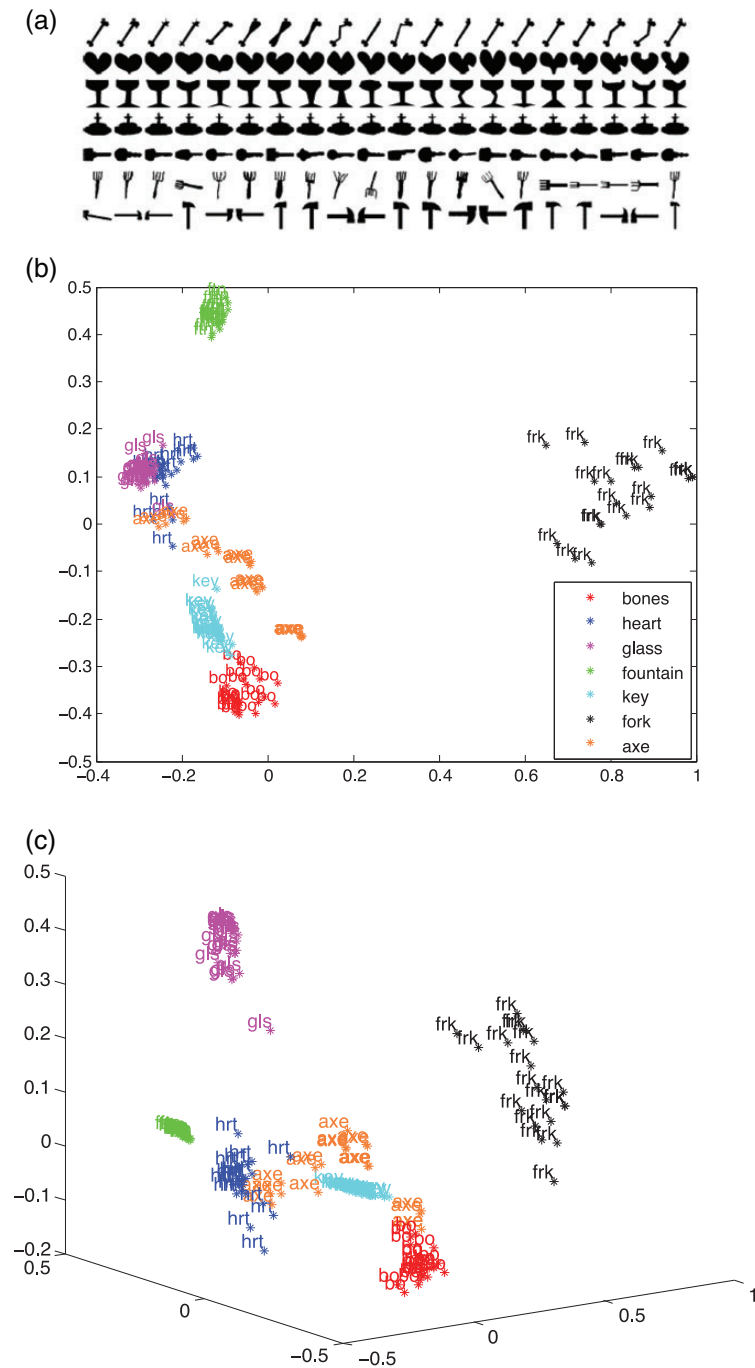


FIG. 11. (a) The subset of the silhouette database. Each row corresponds to one of the objects: Bone, Heart, Glass, Fountain, Key, Fork and Axe. Note that while the objects are distinct, there is a great deal of variation within each object. (b) The two-dimensional projection using multidimensional scaling. The classes are Bone in red, Heart in blue, Glass in magenta, Fountain in green, Key in cyan, Fork in black and Axe in orange. (c) The three-dimensional projection using multidimensional scaling.

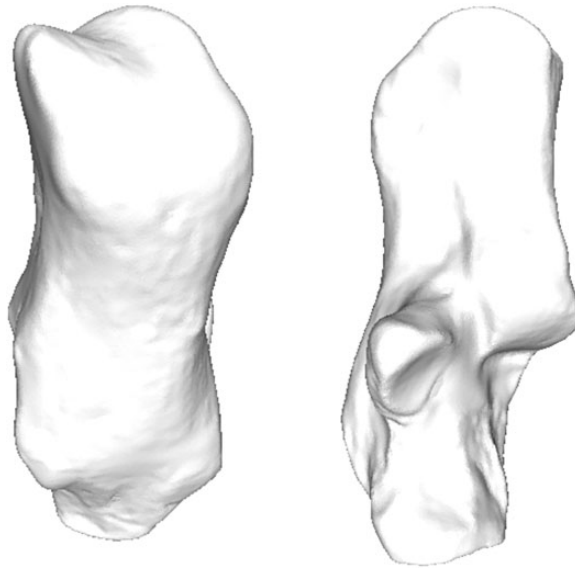


FIG. 12. Images of a calcaneus from two different angles.

phenotypes such as bones. A challenge in modeling phenotypic variation is developing automated methods to measure the variation or distance between shapes [8,9,23].

The data consist of heel bones (calcanei) from 106 extant and extinct primates [9,23]. The bones were scanned using microCT scanning and the data for each bone consist of thousands of points in \mathbb{R}^3 . Details can be found in [10]. See Fig. 12 for two pictures of a calcaneus at different angles. See Appendix for a list. From these distances, we constructed a multidimensional scaling plot of the samples with $D = 2$ (see Fig. 13). We compared the pairwise distances between the projections of the bones by three methods:

- (i) Manual: The original analysis of this sample in Gladman *et al.* [23] was based on 27 manually placed landmarks per bone. The landmark coordinates were then scaled and aligned by a generalized Procrustes superimposition and finally analyzed with principal coordinates analysis. We then projected the samples onto the first two principal coordinates.
- (ii) Automated protocol: An automated method was developed in [31] to compute distances between bones as well as to align the bones to standard orientation. This alignment protocol also outputs pairwise Procrustes distances based on 1000 automatically positioned pseudolandmarks. These pairwise distances can then be projected onto two principal coordinates.
- (iii) PHT: We first aligned the bones using the same procedure as in the automated protocol above. We then computed pairwise distances between bones using the PHT. These pairwise distances can then be projected onto two principal coordinates.

Given these three analyses of the same 106 bones projected into two dimensions. We compared the distances between corresponding bones for each projection by optimizing for rotation, and translation. This was done using the iterative closest point (ICP) algorithm [4], which takes two point sets and

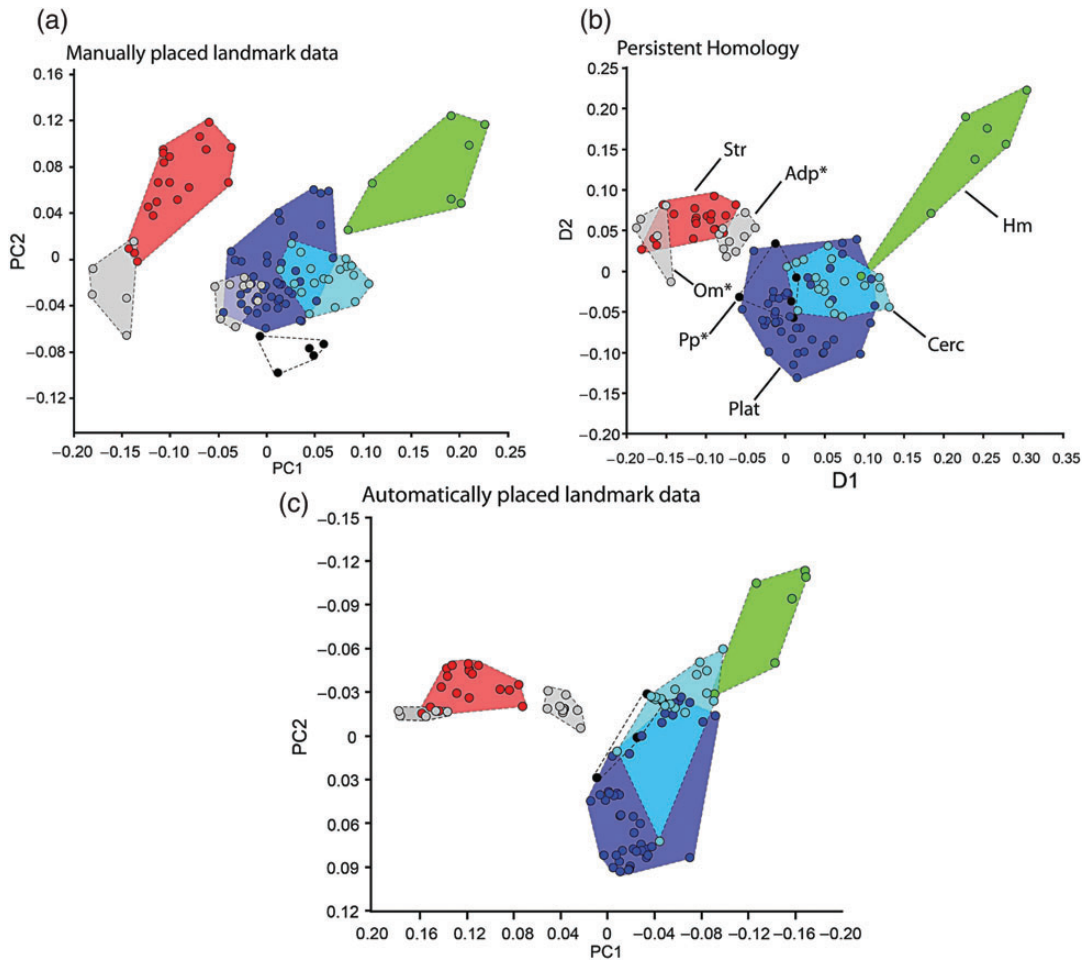


FIG. 13. Phenetic clustering of phylogenetic groups of primate calcanei ($n = 106$). 67 genera are represented. See Appendix for specimen information. Asterisks indicate groups of extinct taxa. Abbreviations: Str, Strepsirrhines; Plat, platyrrhines; Cerc, Cercopithecoidea; Om, Omomyiforms; Adp, Adapiforms; Pp, parapithecids; Hmn, Hominoidea. Note that more primitive prosimian taxa cluster separately from simians (Om, Adp, Str.). Also note that monkeys (Plat, Cerc, Pp) cluster mainly separately from apes (Hmn). This is virtually the same type of clustering observed with more labor intensive (and fundamentally subjective) manually collected landmarks. The position of adapiforms between strepsirrhines and platyrrhines is consistent with previous descriptions of the phenetic affinities of this group. (a) Using the manual alignment method, (b) using the PHT method, (c) the automated landmark-based method.

computes the optimal rotation and translation to align the point sets. We compared the combined Euclidean distance between the aligned points between each distance computation method:

- (1) Distance between automated protocol and PHT: 0.014
- (2) Distance between manual and automated protocol: 0.015
- (3) Distance between manual and PHT: 0.016.

The two automated methods seem to be closer to each other than the manual landmark-based method. It should be recalled here that we used the same alignment processes for both the automated and the

PHT—if we had used a different alignment process, such as that in Section 3.4, we would have subtlety affected the distances. In addition, the distance between the PHT transform and the manual protocol is greater than the distance between the automated protocol and the manual protocol. Results of MDS on all three distances are displayed in Fig. 13. A qualitative analysis suggests that the PHT distances may be outperforming the other two methods.

5. Discussion

In this paper, we stated the PHT as a statistic to capture information in a shape. Our main result is to prove that this transform is injective. Two useful features of our method is that we do not require user-specified landmarks, and we also can measure distances between shapes that are not isomorphic since we are using topological features.

Several questions remain regarding this approach including the following:

- (1) we suspect that our injectivity results using a constructive method will extend to simplicial complexes lying in Euclidean spaces for dimensions > 3 and to more general compact subsets of Euclidean space such as manifolds. However, we do not have a proof;
- (2) we want to investigate the details of a supervised learning approach using finitely many directions—how the construction works and what error could there be in this reconstruction.
- (3) We are very interested in developing more robust methods for aligning objects. The method for accounting for rotation in Section 3.4 is too computationally heavy for surfaces in \mathbb{R}^3 , but reasonable for shapes in \mathbb{R}^2 ;
- (4) can we examine the injectivity of other geometric and topological summaries of the data and use this to better understand classic shape space models.

Acknowledgement

K.T. thanks Shmuel Weinberger for helpful conversations. S.M. thank Jesus Puente, Ingrid Daubechies and Jenny Tung for useful comments. S.M. also thanks W. Mio and L. Ma for Fig. 10.

Funding

This work was supported by the National Institutes of Health (Systems Biology): [5P50-GM081883, AFOSR: FA9550-10-1-0436 and NSF CCF-1049290 all to SM].

REFERENCES

1. AGARWAL, P. K., EDELSBRUNNER, H., HARER, J. & WANG, Y. (2004) Extreme elevation on a 2-manifold. *Proc. 20th Annu. Sym. Comput. Geom.* (J.-D. Boissonnat & J. Snoeyink eds), pp. 357–365.
2. BANDULASIRI, A., BHATTACHARYA, R. N. & PATRANGENARU, V. (2009) Nonparametric inference for extrinsic means on size-and-(reflection)-shape manifolds with applications in medical imaging. *J. Multivariate Anal.*, **100**, 1867–1882.
3. BERGER, J. O. & WOLPERT, R. L. (1988) *The Likelihood Principle*. 2nd edn. Hayward, California: Institute of Mathematical Statistics.
4. BESL, P. J. & MCKAY, N. D. (1992) A method for registration of 3-D shapes. *IEEE Trans. Pattern Anal. Mach. Intell.*, **14**, 239–256.
5. BHATTACHARYA, A. & BHATTACHARYA, R. N. (2008) Statistics on Riemannian manifolds: asymptotic distribution and curvature. *Proc. Am. Math. Soc.*, **136**, 2959–2967.

6. BHATTACHARYA, R. N. & PATRANGENARU, V. (2005) Large sample theory of intrinsic and extrinsic sample means on manifolds-II. *Ann. Statist.*, **33**, 1225–1259.
7. BOOKSTEIN, F. L. (1997) *Morphometric Tools for Landmark Data: Geometry and Biology*. Cambridge: Cambridge University Press.
8. BOYER, D. M., LIPMAN, Y., CLAIR, E. ST., PUENTE, J., PATEL, B. A., FUNKHOUSER, T., JERNVALL, J. & DAUBECHIES, I. (2011) Algorithms to automatically quantify the geometric similarity of anatomical surfaces. *Proc. Natl. Acad. Sci.*, **108**, 18221–18226.
9. BOYER, D. M., PUENTE, J., GLADMAN, J. T., GLYNN, C., MUKHERJEE, S. & DAUBECHIES, I. (2014) A new fully automated approach for aligning and comparing shapes. *Anatomical Rec.* (in press).
10. BOYER, D. M. & SEIFFERT, E. R. (2013) Patterns of Astragalar Fibular facet orientation in extant and fossil primates and their evolutionary implications. *Am. J. Phys. Anthropol.*, **151**, 420–447.
11. BUBENIK, P., CARLSSON, G., KIM, P. T. & LUO, Z.-M. (2010) Statistical topology via Morse theory, persistence, and nonparametric estimation. *Algebraic Methods in Statistics and Probability II*. Contemporary Mathematics, vol. 516, pp. 75–92.
12. CARLSSON, G. (2009) Topology and data. *Bull. Am. Math. Soc.*, **46**, 255–308.
13. COHEN-STEINER, D., EDELSBRUNNER, H. AND HARER, J. (2007) Stability of persistence diagrams. *Discrete Comput. Geom.*, **37**, 103–120.
14. DE SILVA, V. & GHRIST, R. (2007) Homological sensor networks. *Not. Am. Math. Soc.*, **54**, 10–17.
15. DE SILVA, V., MOROZOV, D. & VEJDEMO-JOHANSSON, M. (2011) Dualities in persistent (co) homology. *Inverse Probl.*, **27**(LBNL-5237E), 124003.
16. DIGGLE, P. J. (2003) *Statistical Analysis of Spatial Point Patterns*. Oxford: Oxford University Press.
17. DRYDEN, I. L., LE, H., PRESTON, S. & WOOD, A. T. A. (2014) Mean shapes, projections and intrinsic limiting distributions. *J. Stat. Plan. Inference*, **145**, 25–32.
18. DRYDEN, I. L. & MARDIA, K. V. (1998) *Statistical Shape Analysis*. Wiley Series in Probability and Statistics. Hoboken, NJ: Wiley.
19. DUPUIS, P. & GRENANDER, U. (1998) Variational problems on flows of diffeomorphisms for image matching. *Q. Appl. Math.*, **LVI**, 587–600.
20. EDELSBRUNNER, H. & HARER, J. (2010) *Computational Topology: An Introduction*. Providence, RI: American Mathematical Society.
21. GAMBLE, J. & HEO, G. (2010) Exploring uses of persistent homology for statistical analysis of landmark-based shape data. *J. Multivariate Anal.*, **101**, 2184–2199.
22. GAO, J. X. (2004) Visionlab. http://visionlab.uta.edu/shape_data.htm
23. GLADMAN, J. T., BOYER, D. M., SIMONS, E. L. & SEIFFERT, E. R. (2013) A calcaneus attributable to the primitive late eocene anthropoid *Proteopithecus sylviae*: phenetic affinities and phylogenetic implications. *Am. J. Phys. Anthropol.*, **151**, 372–397.
24. KENDALL, D. G. (1977) The diffusion of shape. *Adv. Appl. Prob.*, **9**, 428–430.
25. KENDALL, D. G. (1984) Shape manifolds, procrustean metrics, and complex projective spaces. *Bull. Lond. Math. Soc.*, **16**, 81–121.
26. KLAİN, D. A. & ROTA, G. C. (1997) *Introduction to Geometric Probability*. Cambridge: Lezioni Lincee, Cambridge University Press.
27. KRUSKAL, J. B. & WISH, M. (1978) *Multidimensional Scaling*. Number 11 in 07. Newbury Park, CA: SAGE Publications.
28. LATECKI, L. J., LAKÄMPER, R. & ECKHARDT, U. (2000) Shape descriptors for non-rigid shapes with a single closed contour. *Proc. IEEE Conf. Computer Vision and Pattern Recognition*, pp. 424–429.
29. LIPMAN, Y., AL-AIFARI, R. & DAUBECHIES, I. (2013) Continuous procrustes distance between two surfaces. *Commun. Pure Appl. Math.*, **66**, 934–963.
30. MOLLER, J. & WAAGEPETERSEN, R. (2003) *Statistical Inference for Spatial Point Processes*. Chapman & Hall.
31. PUENTE, J. (2013) Distances and algorithms to compare sets of shapes for automated biological morphometrics. *Ph.D. Thesis*, Princeton University.
32. RIPLEY, B. D. (1976) The second-order analysis of stationary point processes. *Ann. Appl. Prob.*, **13**, 255–266.

33. SCHAPIRA, P. (1991) Operations on constructible functions. *J. Pure Appl. Algebra*, **72**, 83–93.
34. SCHAPIRA, P. (1995) Tomography of constructible functions. *Applied Algebra, Algebraic Algorithms and Error-Correcting Codes* (G. Cohen, M. Giusti & T. Mora eds). Lecture Notes in Computer Science, vol. 948. Heidelberg, Berlin: Springer, pp. 427–435.
35. SCHMIDLER, S. C. (2007) Fast Bayesian shape matching using geometric algorithms. *Bayesian Statistics 8* (J. Bernardo, M. Bayarri, J. Berger, A. Dawid, D. Heckerman & A. Smith eds). Oxford: Oxford University Press, pp. 1–20.
36. SIKORA, T. (2001) The MPEG-7 visual standard for content description—an overview. *IEEE Trans. Circuits Syst. Video Technol.*, **11**, 696–702.
37. STOYAN, D., KENDALL, W. S. & MECKE, J. (1987) *Stochastic Geometry and its Applications*. Wiley Series in Probability and Mathematical Statistics: Applied Probability and Statistics. Chichester: John Wiley & Sons Ltd. With a foreword by D. G. Kendall.
38. STYNER, M., OGUZ, I., XU, S., BRECHBULER, C., PANTAZIS, D. & GERIG, G. (1984) Framework for the statistical shape analysis of brain structures using SPHARM-PDM. *Insight J.*, **1071**, 242–250.
39. TURNER, K. (2013) Means and medians of sets of persistence diagrams. ArXiv e-prints.
40. TURNER, K., MILEYKO, Y., MUKHERJEE, S. & JOHN, H. (2014) Fréchet means for distributions of persistence diagrams. *Discrete Comput. Geom.*, **52**, 44–70.
41. VILLANI, C. (2009) *Optimal Transport: Old and New*, vol. 338. Berlin, Heidelberg, New York: Springer.
42. WANG Y., AGARWAL, P. K., BROWN, P. & EDELSBRUNNER, H. (2005) Fast geometric algorithm for rigid protein docking. *Proc. 10th. Pacific Symposium on Biocomputing (PSB)* (R. B. Altman, A. K. Dunker, L. Hunter, T. A. Jung & T. E. Klein eds), pp. 64–75.
43. WORSLEY, K. J. (1995) Boundary corrections for the expected euler characteristic of excursion sets of random fields, with an application to astrophysics. *Adv. Appl. Prob.*, 943–959.
44. WORSLEY, K. J. (1995) Estimating the number of peaks in a random field using the Hadwiger characteristic of excursion sets, with applications to medical images. *Ann.Stat.*, **23**, 640–669. Mathematical Reviews number (MathSciNet): MR1332586; Zentralblatt MATH identifier: 0898.62120.
45. ZELDITCH, M. L., SWIDERSKI, D. L., SHEETS, D. H. & FINK, W. L. (2004) *Geometric Morphometrics for Biologists*, 1st edn. Waltham, MA: Academic Press.

Appendix A. Calcaneal data set

Full calcaneal data set. Bone # column can be used to look up specimens in the 3D alignment file.

Taxon	Specimen ID	Bone no.
<i>Avahi laniger</i>	AMNH 170461	1
<i>Cheirogaleus major</i>	AMNH 100640	2
<i>Daubentonia madagascariensis</i>	AMNH 185643	3
<i>Eulemur fulvus</i>	AMNH 17403	4
<i>Eulemur fulvus</i>	AMNH 31254	5
<i>Hapalemur griseus</i>	AMNH 170675	6
<i>Hapalemur griseus</i>	AMNH 170689	7
<i>Hapalemur griseus</i>	AMNH 61589	8
<i>Indri indri</i>	AMNH 100504	9
<i>Indri indri</i>	AMNH 208992	10
<i>Lemur catta</i>	AMNH 150039	11

Taxon	Specimen ID	Bone no.
<i>Lemur catta</i>	AMNH 170739	12
<i>Lemur catta</i>	AMNH 22912	13
<i>Lepilemur mustelinus</i>	AMNH 170565	14
<i>Lepilemur mustelinus</i>	AMNH 170568	15
<i>Lepilemur mustelinus</i>	AMNH 170569	16
<i>Propithecus verreauxi</i>	AMNH 170463	17
<i>Propithecus verreauxi</i>	AMNH 170491	18
<i>Varecia variegata</i>	AMNH 100512	19
<i>Alouatta seniculus</i>	AMNH 42316	20
<i>Alouatta seniculus</i>	SBU NA113	21
<i>Alouatta</i> sp.	SBU NA117	22
<i>Alouatta</i> sp.	SBU NA118	23
<i>Aotus azarae</i>	AMNH 211482	24
<i>Aotus infulatus</i>	AMNH 94992	25
<i>Aotus</i> sp.	AMNH 201647	26
<i>Ateles paniscus</i>	SBU NA110	27
<i>Ateles</i> sp.	SBU NA113	28
<i>Ateles</i> sp.	SBU NA118	29
<i>Brachyteles arachnoides</i>	AMNH 260	30
<i>Cacajao calvus</i>	AMNH 70192	31
<i>Cacajao calvus</i>	SBU NCj1	32
<i>Callicebus donacophilus</i>	AMNH 211490	33
<i>Callicebus moloch</i>	AMNH 244363	34
<i>Callicebus moloch</i>	AMNH 94977	35
<i>Callimico goeldi</i>	AMNH 183289	36
<i>Callimico goeldi</i>	SBU NCa1	37
<i>Callithrix jacchus</i>	AMNH 133692	38
<i>Callithrix jacchus</i>	AMNH 133698	39
<i>Cebuella pygmaea</i>	AMNH 244101	40
<i>Cebuella pygmaea</i>	SBU NC1	41
<i>Cebus apella</i>	SBU NCb4	42
<i>Cebus</i> sp.	SBU NCb5	43
<i>Chiropotes satanus</i>	AMNH 95760	44
<i>Chiropotes satanus</i>	AMNH 96123	45
<i>Chiropotes</i> sp.	SBU NCh2	46
<i>Leontopithecus rosalia</i>	AMNH 137270	47
<i>Leontopithecus rosalia</i>	AMNH 60647	48
<i>Pithecia monachus</i>	AMNH 187978	49
<i>Pithecia pithecia</i>	AMNH 149149	50
<i>Saguinus midas</i>	AMNH 266481	51
<i>Saguinus mystax</i>	AMNH 188177	52
<i>Saguinus</i> sp.	SBU NSg12	53
<i>Saguinus</i> sp.	SBU NSg2	54
<i>Saimiri boliviensis</i>	AMNH209934	55
<i>Saimiri boliviensis</i>	AMNH211650	56
<i>Saimiri boliviensis</i>	AMNH211651	57
<i>Saimiri sciureus</i>	AMNH188080	58
<i>Saimiri</i> sp.	SBU NSm2	59

Taxon	Specimen ID	Bone no.
<i>Cercopithecus</i> sp.	SBU No Number	60
<i>Cercopithecus</i> sp.	SBU No Number	61
<i>Chlorocebus aethiops</i>	SBU OC7	62
<i>Chlorocebus cynosuros</i>	AMNH 80787	63
<i>Colobus geureza</i>	AMNH 27711	64
<i>Erythrocebus patas</i>	AMNH 34709	65
<i>Lophocebus albigena</i>	AMNH 52603	66
<i>Macaca nigra</i>	SBU OCn1	67
<i>Macaca tonkeana</i>	AMNH 153402	68
<i>Mandrillus sphinx</i>	AMNH 89367	69
<i>Nasalis larvatus</i>	AMNH 106272	70
<i>Papio hamadryas</i>	AMNH 80774	71
<i>Piliocolobus badius</i>	AMNH 52303	72
<i>Piliocolobus badius</i>	ED 4651	73
<i>Pygathrix nemaeus</i>	AMNH 87255	74
<i>Theropithecus gelada</i>	AMNH 201008	75
<i>Trachypithecus obscurus</i>	AMNH 112977	76
<i>Gorilla</i> sp.	AD 6001	77
<i>Hylobates lar</i>	AMNH 119601	78
<i>Pan troglodytes</i>	AMNH 51202	79
<i>Pan troglodytes</i>	AMNH 51278	80
<i>Pongo pygmaeus</i>	AMNH 28253	81
<i>Symphalangus syndactylus</i>	AMNH 106583	82
<i>Cantius abditus</i>	USGS 6783	83
<i>Cantius</i> sp.	USGS 6774	84
<i>Cantius trigonodus</i>	AMNH 16852	85
<i>Cantius trigonodus</i>	USGS 21829	86
<i>Cebupithecia sarmientoi</i>	UCMP 38762*	87
<i>Marcgodinotius indicus</i>	GU 709	88
<i>Mesopithecus pentelici</i>	MNHN PIK-266*	89
<i>Neosaimiri fieldsi</i>	IGM-KU 89202*	90
<i>Neosaimiri fieldsi</i>	IGM-KU 89203*	91
<i>Notharctus</i> sp.	AMNH 55061	92
<i>Notharctus tenebrosus</i>	AMNH 11474	93
<i>Omomyid</i>	AMNH 29164	94
<i>Omomys</i> sp.	UM 98604	95
<i>Oreopithecus bambolii</i>	NMB 37*	96
<i>Ourayia uintensis</i>	SDNM 60933	97
<i>Parapithecoid</i>	DPC 15679	98
<i>Parapithecoid</i>	DPC 20576	99
<i>Parapithecoid</i>	DPC 2381	100
<i>Parapithecoid</i>	DPC 8810	101
<i>Proteopithecus sylviae</i>	DPC 23662A	102
<i>Smilodectes gracilis</i>	AMNH131763	103
<i>Smilodectes gracilis</i>	AMNH131774	104
<i>Teihardina belgica</i>	IRSNB 16786-03	105
<i>Washakius insignis</i>	AMNH 88824	106

Appendix B. Examples of PHT of families of surfaces

The purpose of this appendix is to examine in detail the process of the PHT of some parameterized families of shapes and also to consider the distances between the PHTs of these shapes. This should help the reader gain an intuition about the PHT. We will consider quadric ellipsoids and hyperboloids which have had restricted z -values. We will explain what the persistence diagrams in each direction are. In the first case (ellipsoids), we will consider the normalization process. We will calculate the distances between the PHTs for sets within these families and analyze the results using multidimensional scaling. We also, in the case of ellipsoids, compare the values of the distances found by Algorithm 4.1 of a surface mesh to the value using the exact algebraic set and computed by numerical integration. Showing that these values are close reassures that we are not losing too much information by taking finite approximations (both in the surface mesh stage and the finitely many directions instead of an integral stage). The code used to compute the PHTs of the surface meshes, and the distances between them, within these examples is available on the journal's website.

B.1 PHT of ellipsoids

Let $E(a, b, c)$ denote the ellipsoid with Cartesian equation:

$$\frac{x^2}{a^2} + \frac{y^2}{b^2} + \frac{z^2}{c^2} = 1.$$

The algebraic description of the ellipsoids means that it is possible for us to find formulas to describe the persistent homology diagrams for the height functions in each direction. Fix a direction described by the unit vector $v = (v_1, v_2, v_3)$.

The $X_1(E(a, b, c), v)$ in the PHT of $E(a, b, c)$ has no off-diagonal points for all $v \in S^2$. The $X_0(E(a, b, c), v)$ and $X_2(E(a, b, c), v)$ each have exactly one off-diagonal point. These correspond to the essential classes of the ellipsoid. The H_0 class appearing when the ellipsoid is first contacted and the H_2 class appearing when the entire ellipsoid is completed. Thus, to compute these diagrams, it is enough to compute the minimum and maximum value of

$$f(x, y, z) := xv_1 + yv_2 + zv_3$$

for $(x, y, z) \in E(a, b, c)$, that is (x, y, z) that satisfy

$$g(x, y, z) := \frac{x^2}{a^2} + \frac{y^2}{b^2} + \frac{z^2}{c^2} = 1.$$

Geometrically this occurs when the normal to the surface is $\pm v$.

Using the method of Lagrange multipliers, the PHT of $E(a, b, c)$ is calculated to be⁴

$$X_0(E(a, b, c), (v_1, v_2, v_3)) = \{(-\sqrt{a^2v_1^2 + b^2v_2^2 + c^2v_3^2}, \infty)\},$$

$$X_1(E(a, b, c), (v_1, v_2, v_3)) = \{\},$$

$$X_2(E(a, b, c), (v_1, v_2, v_3)) = \{(\sqrt{a^2v_1^2 + b^2v_2^2 + c^2v_3^2}, \infty)\},$$

⁴ Note here that we are recording the persistence diagrams by listing the off-diagonal points. They also contain countably infinite copies of the diagonal.

We may or may not wish to normalize the ellipses. By symmetry these ellipsoids are already centered. If we were to normalize them with respect to size by the process described in Section 3.4, we would need to calculate, for each $E(a, b, c)$, the scaling factor

$$I(a, b, c) = \frac{1}{4\pi} \int_{\beta=-\pi}^{\pi} \int_{\alpha=-\pi/2}^{\pi/2} \sqrt{c^2 \sin^2 \alpha + \cos^2 \alpha (a^2 \cos^2 \beta + b^2 \sin^2 \beta)} \cos \alpha \, d\alpha \, d\beta. \quad (\text{B.1})$$

All our integrals over the sphere are done in the polar coordinates $(\alpha, \beta) \mapsto (\cos \alpha \cos \beta, \cos \alpha \sin \beta, \sin \alpha)$. The Jacobian for this parameterization is $\cos \alpha$. Unfortunately, the integral in (B.1) does not have a nice closed form, so we must use numerical integration to compute it. Given a triple (a, b, c) , we can rescale $E(a, b, c)$ to find a normalized (with respect to size) ellipsoid

$$\hat{E}(a, b, c) = E\left(\frac{a}{I(a, b, c)}, \frac{b}{I(a, b, c)}, \frac{c}{I(a, b, c)}\right).$$

To find the distances between the centered and normalized ellipses, we would then need to consider pairwise the different distances under all alignments and take the minimal one.

We looked at a set of ellipsoids

$$\{E(a, b, c) : a, b, c \in \{1, 2, 3, 4, 5\}\},$$

with their size and location in space fixed. We computed all the pairwise distances and then performed multidimensional scaling to the matrix of distances squared that resulted. After applying multidimensional scaling, there were natural geometric interpretations of the coordinates. Furthermore, since ellipsoids are such nice algebraically defined sets, it is possible to have formulae for the persistence diagrams. This allows us to find the true distance between the PHTs by (numerical) integration. We also computed the distances using the algorithm outlined in Section 4.1. By computing the distances in these two ways, we can see how much error is introduced (in this example) through the finite approximations of the surface by using a finite surface mesh and through the finite approximation of integral over the sphere by averaging using a finite number of directions. The relative error of the computed distances by the two different methods of computation was bounded by 0.0532. The relative error was always positive (the algorithm always underestimated the distances compared with the distances computed by the integral) with a mean of 0.0244.

We now will show in detail the computation involved. Let $E_1 = E(a_1, b_1, c_1)$ and $E_2 = E(a_2, b_2, c_2)$. The symmetry of the ellipsoids implies that

$$\text{dist}(X_0(E_1, \nu), X_0(E_2, \nu)) = \text{dist}(X_2(E_1, \nu), X_2(E_2, \nu))$$

for all $\nu \in S^2$. Also none of the $X_1(E_i, \nu)$ has any off-diagonal points and hence

$$\int \text{dist}(X_1(E_1, \nu), X_1(E_2, \nu)) \, d\nu = 0.$$

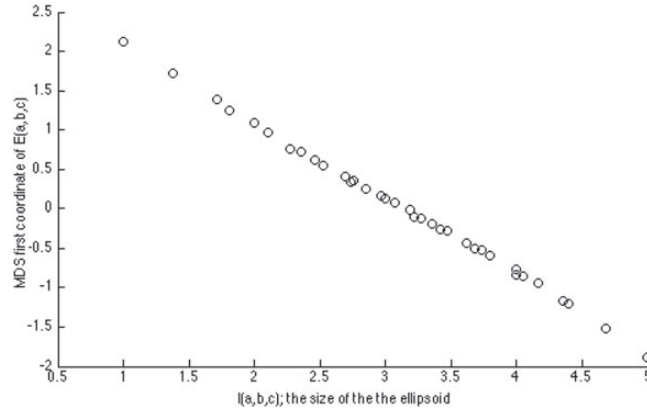


FIG. B1. The first coordinate of the MDS for $E(a, b, c)$ is close to a linear function for $I(a, b, c)$ (the size of the ellipsoid).

Together these simplify the calculation of $\text{dist}(E_1, E_2)$.

$$\begin{aligned}
 \text{dist}(E_1, E_2) &= \frac{2}{\text{vol}(S^2)} \int_{v \in S^2} \text{dist}(X_0(E_1, v), X_0(E_2, v)) \, dv \\
 &= \frac{2}{4\pi} \int_{\beta=-\pi}^{\pi} \int_{\alpha=-\pi/2}^{\pi/2} d(X_0(E_1, v(\alpha, \beta)), X_0(E_2, v(\alpha, \beta))) \cos \alpha \, d\alpha \, d\beta \\
 &= \frac{2}{4\pi} \int_{\beta=-\pi}^{\pi} \int_{\alpha=-\pi/2}^{\pi/2} |\sqrt{c_1^2 \sin^2 \alpha + \cos^2 \alpha (a_1^2 \cos^2 \beta + b_1^2 \sin^2 \beta)} \\
 &\quad - \sqrt{c_2^2 \sin^2 \alpha + \cos^2 \alpha (a_2^2 \cos^2 \beta + b_2^2 \sin^2 \beta)}| \cos \alpha \, d\alpha \, d\beta.
 \end{aligned}$$

For the set of ellipsoids $\{E(a, b, c) : a, b, c \in \{1, 2, 3, 4, 5\}\}$, we computed the distance matrix by the formula above and performed multidimensional scaling to this distance matrix. This analysis seemed to show that these PHTs of ellipsoids effectively lie in a three-dimensional space. The first dimension (that is corresponding to the highest eigenvalue) is close to a linear function of the size of the ellipsoid (as measured by $I(a, b, c)$ as calculated in Equation (B.1)). This is illustrated in Fig. B1.

In the next two dimensions, the vector of direction is symmetric in relation to the ratios of a , b and c . When $a = b = c$, that is, we have a sphere, the values of the second and third coordinates are both zero. When the ratios are equal, then the points lie in the same direction. In Fig. B2, we have plotted the second and third coordinates from the multidimensional scaling analysis. The eigenvalues corresponding to these two dimensions were equal, so the choice of coordinates in this plane was arbitrary.

B.2 PHT of hperboloids with restricted z -values

Now we will consider a family of hyperboloids with restricted z -values—cut-off hyperboloids. By this, we mean sets of shapes of the form

$$\text{Hyp}(a, b, c) := \left\{ (x, y, z) : \frac{x^2}{a^2} + \frac{y^2}{b^2} - \frac{z^2}{c^2} = 1 \text{ and } z \in [-1, 1] \right\}.$$

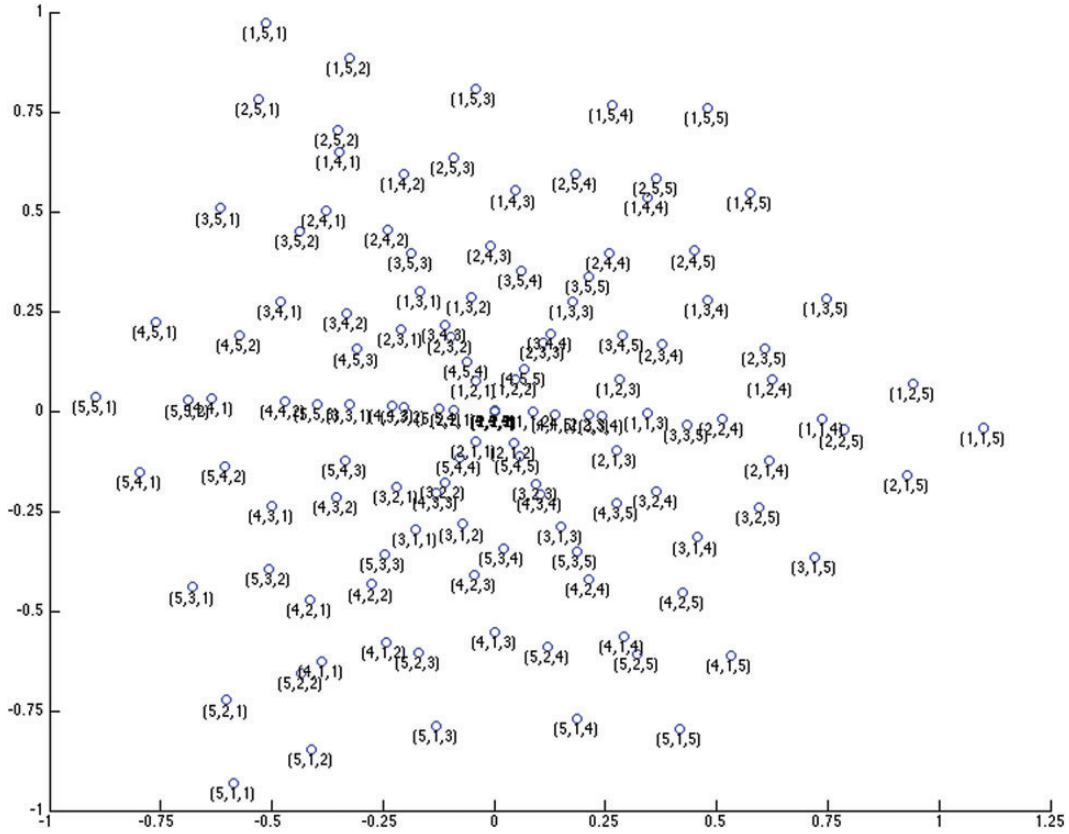


FIG. B2. The plot of the second and third MDS scores for the set of ellipsoids.

Each $\text{Hyp}(a, b, c)$ is a surface whose boundary is the pair of ellipses $\{(x, y, 1) : x^2/a^2 + y^2/b^2 = 1 + 1/c^2\}$ and $\{(x, y, -1) : x^2/a^2 + y^2/b^2 = 1 + 1/c^2\}$. An example of such a surface is drawn in Fig. B3.

We will now examine what the persistence diagrams that correspond to the height function in direction v are, where v is a unit vector (v_1, v_2, v_3) with $v_1, v_2, v_3 \geq 0$. By symmetry, we can then deduce the rest of the PHT. Let $M = \text{Hyp}(a, b, c)$. Recall that to compute $\text{PHT}(M)(v)$, we care about the filtration of subsets of the form $M(v)_r := \{(x, y, z) \in M : (x, y, z) \cdot v \leq r\}$. Changes in homology as we progress through this subset can occur only when either first contacting or completing one of the boundary ellipses or when the $M(v)_r$ encounters a point in M whose normal is $\pm v$. We will now discuss each of these scenarios and find formulae for at what heights they occur.

Let $r_{l,1}$ and $r_{l,2}$, and $r_{u,1}$ and $r_{u,2}$, be the heights that $M(v)_r$ first contacts and then completes the lower- and upper-boundary ellipses, respectively. To compute $r_{l,1}$ and $r_{l,2}$, or $r_{u,1}$ and $r_{u,2}$, we can use the method of Lagrange multipliers where we wish to find the extreme values of $f_l(x, y) = v_1x + v_2y - v_3$, or $f_u(x, y) = v_1x + v_2y + v_3$, with the constraint that $g(x, y) = (x^2/a^2) + (y^2/b^2) = (1 + 1/c^2)$. The formulae we calculated are in Table B1.

For some directions v there will exist points (x_1, y_1, z_1) and (x_2, y_2, z_2) in M with normal $\pm v$. If they exist, denote the heights at which $M(v)_r$ encounters such points by $r_{i,1}$ and $r_{i,2}$. If they exist, such

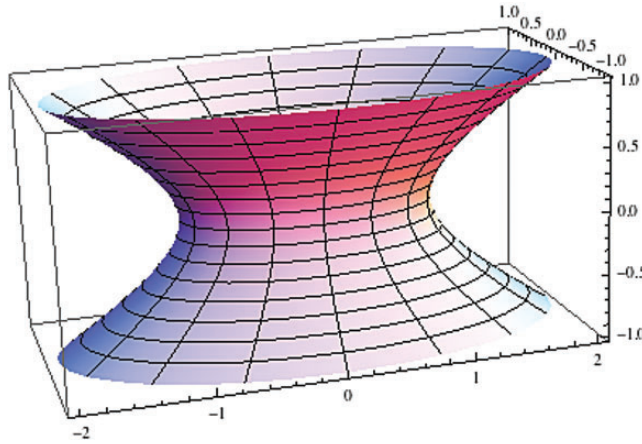


FIG. B3. A cut-off hyperboloid.

TABLE B1 *Table of the heights at which homological changes may happen*

	$j = 1$	$j = 2$
$r_{lj}(v, a, b, c)$	$-\sqrt{1 + \frac{1}{c^2} \sqrt{a^2 v_1^2 + b^2 v_2^2}} - v_3$	$\sqrt{1 + \frac{1}{c^2} \sqrt{a^2 v_1^2 + b^2 v_2^2}} - v_3$
$r_{uj}(v, a, b, c)$	$-\sqrt{1 + \frac{1}{c^2} \sqrt{a^2 v_1^2 + b^2 v_2^2}} + v_3$	$\sqrt{1 + \frac{1}{c^2} \sqrt{a^2 v_1^2 + b^2 v_2^2}} + v_3$
$r_{ij}(v, a, b, c)$ (if it occurs)	$-\sqrt{a^2 v_1^2 + b^2 v_2^2 - c^2 v_3^2}$	$\sqrt{a^2 v_1^2 + b^2 v_2^2 - c^2 v_3^2}$

points will satisfy $(2x/a^2, 2y/a^2, 2z/a^2) = \lambda(v - 1, v_2, v_3)$ for some λ . Using the constraint $(x^2/a^2) + (y^2/b^2) - (z^2/c^2) = 1$, we compute these heights (if they exist) and these are shown in Table B1. The corresponding points in M (with normal $\pm v$) have z coordinate $\pm c^2 v_3 / \sqrt{a^2 v_1^2 + b^2 v_2^2 - c^2 v_3^2}$ and hence they exist in the cut-off hyperboloid exactly when $c^2 v_3 / \sqrt{a^2 v_1^2 + b^2 v_2^2 - c^2 v_3^2} < 1$; that is when

$$c^4 v_3^2 < a^2 v_1^2 + b^2 v_2^2 - c^2 v_3^2. \quad (\text{B.2})$$

All non-boundary points in $\text{Hyp}(a, b, c)$ are saddle points and thus they must be critical points of index 1 for the Morse function defined as the height function in the direction of v . Being an index 1 critical points means that including it must change the homology—causing either a decrease in H_0 or an increase in H_1 when it is encountered.

The $X_0(\text{Hyp}(a, b, c), v)$ will always have one essential class which is at $(r_{l,1}, \infty)$. If there are internal points with normal $\pm v$, then the upper-boundary ellipse is contacted before any path from the lower-boundary ellipse to the upper-boundary ellipse is seen. Thus, the upper-boundary first appears as a second connected component. It then joins the first connected component once a path between the boundary ellipses is first completed which is when the first of the two points with normal $\pm v$ is included. The two components merge at height $r_{i,1}$. We thus have the point $(r_{u,1}, r_{i,1})$ as a second off-diagonal point in $X_0(\text{Hyp}(a, b, c), v)$. Figure B4 shows the progression of important sublevel sets of the height function in direction v over a cut-off hyperboloid in this case.

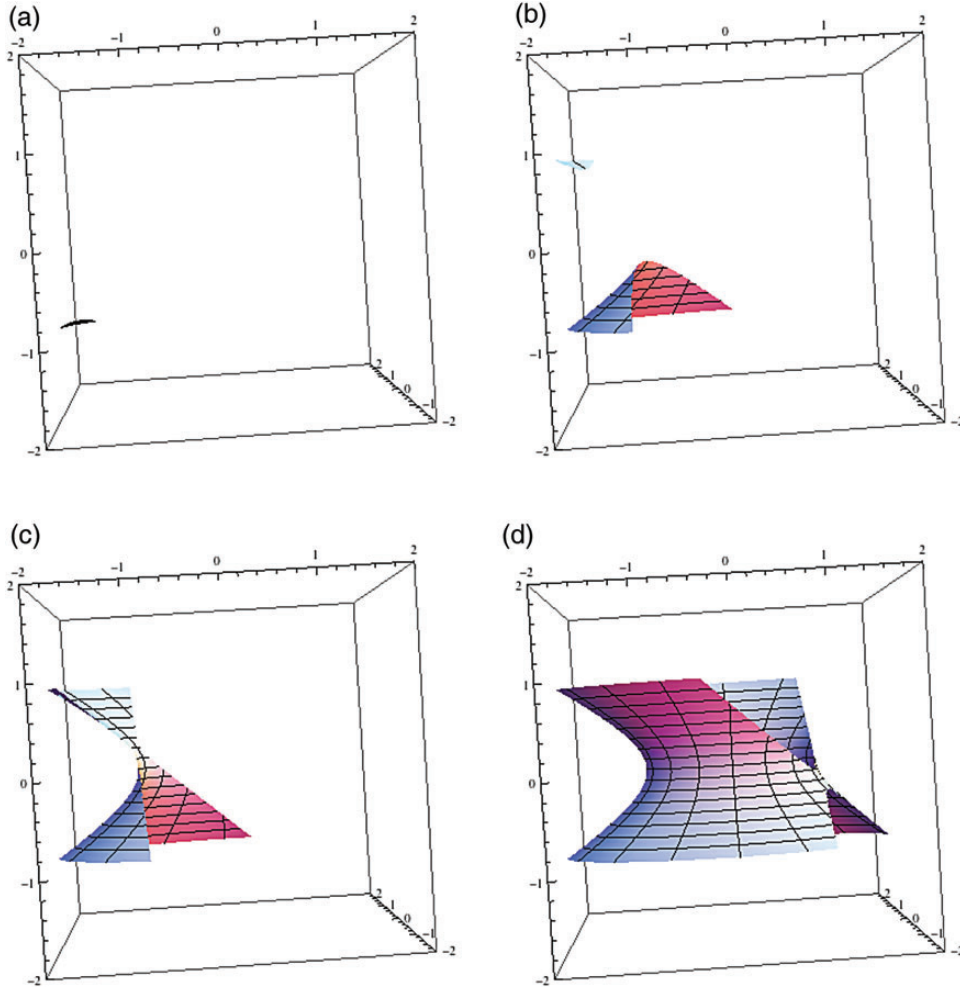
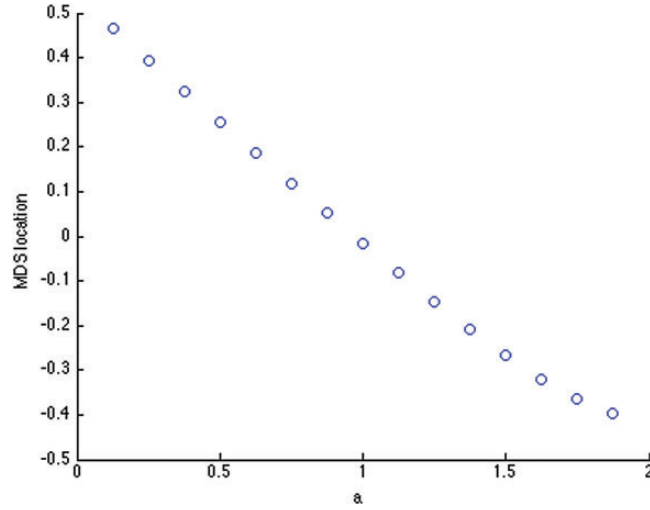


FIG. B4. One possible progression of the sublevel sets of the height function in direction v over a cut-off hyperboloid. (a) The first time a sublevel set is non-empty an essential H_0 class is born. (b) Here the sublevel set touches the upper boundary without containing any path between the upper and lower boundary. A second H_0 persistent homology class is born. (c) A path between the upper and lower boundaries is found—happening when a point on the cut-off hyperboloid has normal $\pm v$. The second H_0 persistent homology class dies. (d) An essential H_1 class is born—happening when another point on the cut-off hyperboloid has normal $\pm v$. No changes in homology occur after this.

There is always exactly one essential class in $X_1(\text{Hyp}(a, b, c), v)$ and no other off-diagonal points. The essential class is born when the loop around the hyperboloid is first completed. If there are internal points with normal v it will occur when the second of these points appears (at height $r_{i,1}$). Otherwise, the loop first appears when the lower-boundary loop is completed (at height $r_{l,2}$). In conclusion, if $c^4 v_3^2 < a^2 v_1^2 + b^2 v_2^2 - c^2 v_3^2$, then

$$X_0(\text{Hyp}(a, b, c), v) = \{(r_{l,1}, \infty), (r_{u,1}, r_{i,1})\}$$

$$X_1(\text{Hyp}(a, b, c), v) = \{(r_{i,2}, \infty)\}$$

FIG. B5. The MDS coordinate of $\text{Hyp}(a)$.

and if $c^4 v_3^2 \geq a^2 v_1^2 + b^2 v_2^2 - c^2 v_3^2$, then

$$X_0(\text{Hyp}(a, b, c), v) = \{(r_{l,1}, \infty)\}$$

$$X_1(\text{Hyp}(a, b, c), v) = \{(r_{l,2}, \infty)\}$$

where the $r_{l,j}$, $r_{u,j}$ and $r_{i,j}$ are the formulae in Table B1.

We now will analyze the distances within a one-dimensional family of cut-off hyperboloids. We will fix the bounding ellipses to be

$$\left\{ (x, y, z) : \frac{x^2}{4} + y^2 = 1 \text{ and } |z| = 1 \right\}.$$

We still have one parameter of freedom. Algebraically, for each $a \in (0, 2)$, we can define a hyperboloid $\text{Hyp}(a) = \text{Hyp}(a, a/2, a/\sqrt{4-a^2})$. These hyperboloids satisfy our desired boundary condition and are determined by where they intersect the x axis; $\text{Hyp}(a)$ intersecting at $\pm(a, 0, 0)$. The advantage of considering this family of cut-off hyperboloids is that they have the same convex hull and hence are already are (up to the same constant scaling factor) normalized.

Again, we will focus on v in the positive quadrant. We have two different cases for what the diagrams are in direction v for $\text{Hyp}(a)$ depending on whether $c^4 v_3^2 < a^2 v_1^2 + b^2 v_2^2 - c^2 v_3^2$ or not. Given our relationships between a, b and c , this condition can be written as $16v_3^2 < (4-a^2)^2(4v_1^2 + v_2^2)$. Importantly, the formulae $r_{u,j}$ and $r_{l,j}$ are independent of a because they only depend on what height the boundary ellipses are contacted or completed, and these boundary ellipses are independent of a .

The $X_1(\text{Hyp}(a), v)$ only contains one essential class regardless of the direction v . Thus, to compute the distance between $X_1(\text{Hyp}(a_1), v)$ and $X_1(\text{Hyp}(a_2), v)$, we just take the distance between the first coordinate of the only point in each diagram. The essential classes in the H_0 persistent homology, for every fixed v , are the same for all of the $\text{Hyp}(a)$, regardless of a , and so when computing the distance between $X_0(\text{Hyp}(a_1), v)$ and $X_0(\text{Hyp}(a_2), v)$, we can effectively ignore them. If both diagrams contain a

finite persistence off diagonal point, then they will have the same birth times (for the fixed direction v) and hence we should match them to each other rather than both to the diagonal.⁵ If only one has a finite persistence off-diagonal point, then it has to be matched to the diagonal.

We computed the distances (with small error due to using a finite approximation) via our algorithm. By inspection of the diagrams in the various cases, we can see that the distance between the PHTs is in fact exactly double the distance between the PH_0 Ts. This would not hold for general cut-off hyperboloids as it stems from having those fixed boundary ellipses. Since the PH_0 Ts are significantly faster to compute, we computed these instead.

We considered the set of shapes $\{\text{Hyp}(a)\}$ for a in 0.125 increments from 0.125 to 1.875. After computing the matrix of distances, we performed MDS. There was only one non-zero eigenvalue. In Fig. B5 we plotted the scores in this coordinate with respect to the variable a .

⁵ This is an advantage of our choice of $p = 1$ in the distance function on the space of persistence diagrams. If we were to use a different metric on the space of persistence diagrams this conclusion (that the two off diagonal point would be paired because they have the same birth time) would not generally hold.